Assimilation of a Coordinated Fleet of Uncrewed Aircraft System Observations in Complex Terrain: EnKF System Design and Preliminary Assessment

ANDERS A. JENSEN,[a] JAMES O. PINTO,[a] SEAN C. C. BAILEY,[b] RYAN A. SOBASH,[a] GIJS DE BOER,[c] ADAM L. HOUSTON,[d] PHILLIP B. CHILSON,[e] TYLER BELL,[e] GLEN ROMINE,[a] SUZANNE W. SMITH,[b] DALE A. LAWRENCE,[f] CORY DIXON,[f] JULIE K. LUNDQUIST,[f,g] JAMEY D. JACOB,[h] JACK ELSTON,[i] SEAN WAUGH,[j] AND MATTHIAS STEINER[a]

[a] *National Center for Atmospheric Research, Boulder, Colorado*
[b] *University of Kentucky, Lexington, Kentucky*
[c] *Cooperative Institute for Research in Environmental Sciences, University of Colorado Boulder, Boulder, Colorado*
[d] *University of Nebraska–Lincoln, Lincoln, Nebraska*
[e] *University of Oklahoma, Norman, Oklahoma*
[f] *University of Colorado Boulder, Boulder, Colorado*
[g] *National Renewable Energy Laboratory, Golden, Colorado*
[h] *Oklahoma State University, Stillwater, Oklahoma*
[i] *Black Swift Technologies, Boulder, Colorado*
[j] *National Severe Storms Laboratory, Norman, Oklahoma*

(Manuscript received 31 October 2020, in final form 4 February 2021)

ABSTRACT: Uncrewed aircraft system (UAS) observations collected during the 2018 Lower Atmospheric Process Studies at Elevation—a Remotely Piloted Aircraft Team Experiment (LAPSE-RATE) field campaign were assimilated into a high-resolution configuration of the Weather Research and Forecasting Model using an ensemble Kalman filter. The benefit of UAS observations was assessed for a terrain-driven (drainage and upvalley) flow event that occurred within Colorado's San Luis Valley (SLV) using independent observations. The analysis and prediction of the strength, depth, and horizontal extent of drainage flow from the Saguache Canyon and the subsequent transition to upvalley and up-canyon flow were improved relative to that obtained both without data assimilation (benchmark) and when only surface observations were assimilated. Assimilation of UAS observations greatly improved the analyses of vertical variations in temperature, relative humidity, and winds at multiple locations in the northern portion of the SLV, with reductions in both bias and the root-mean-square error of roughly 40% for each variable relative to the benchmark run. Despite these noted improvements, some biases remain that were tied to measurement error and/or the impact of the boundary layer parameterization on vertically spreading the observations, both of which require further exploration. The results presented here highlight how observations obtained with a fleet of profiling UAS improve limited-area, high-resolution analyses and short-term forecasts in complex terrain.

KEYWORDS: Complex terrain; Drainage flow; Short-range prediction; Data assimilation; Ensembles; Mesoscale models

1. Introduction

The need for more accurate, higher resolution probabilistic weather guidance spans a range of applications (Dutton 2002). Wind energy companies need high fidelity wind predictions that account for mesoscale and terrain-induced wind variability across a wind farm (Wilczak et al. 2015; Olson et al. 2019b). Precision agriculture requires localized and time-varying predictions of soil moisture, evapotranspiration and winds across farmlands to support more efficient irrigation practices and application of pesticides (Tesfuhuney et al. 2013; Easton et al. 2017). Wildland fire management also requires accurate predictions of how terrain and fuel sources interact with mesoscale flows to influence winds and fire behavior (Coen et al. 2013; Muñoz-Esparza et al. 2018; Jiménez et al. 2018). Emerging modes of autonomous aerial transportation including package delivery by small uncrewed aircraft systems (UAS) and "Urban Air Mobility" mean that decision makers and stakeholders will require a more highly resolved depiction of submesoscale flows (e.g., drainage winds and lake-land breeze circulations) and turbulence structures (Glasheen et al. 2020; Steiner 2019; Garrett-Glaser 2020). To meet these weather guidance needs, the accuracy of mesoscale predictions needs to be improved so that they can be downscaled to provide higher resolution guidance. As such, the distribution of observations of atmospheric state must more closely match the grid spacing of today's operational convection-permitting models.

The emergence of small UAS for use in commercial applications and for atmospheric sensing has grown exponentially over the last decade. Elston et al. (2015) summarized developments in the use of small fixed-wing UAS for sampling boundary layer processes and provided platform-dependent estimates of measurement accuracy. Fixed-wing aircraft can profile the atmosphere (either flying tight spirals or slant paths) or sample spatial variability in atmospheric parameters by flying long horizontal transects at constant altitude (e.g., Elston et al. 2011; Houston et al. 2012). Multirotor aircraft have shown

Corresponding author: Anders A. Jensen, ajensen@ucar.edu

DOI: 10.1175/MWR-D-20-0359.1

great utility in rapidly profiling the lower atmosphere, providing a cost-effective means of monitoring the thermodynamic and kinematic evolution of the boundary layer. These weather-sensing drones are gaining maturity as multirotor aircraft have demonstrated the potential to operate autonomously from launch to landing (Chilson et al. 2019) including automated recharging (Leuenberger et al. 2020). Additional challenges such as the influence of propeller wash on measurement accuracy of temperature and winds near the surface, under conditions of large lapse rates, or near strong inversions have been mitigated significantly though sensor integration studies (Greene et al. 2019). Small UAS have also been lauded for their ability to collect observations in remote locations and extreme environments ranging from icing conditions and severe cold in the polar regions (Curry et al. 2004; Cassano 2014; de Boer et al. 2018) to the corrosive, wet and turbulent boundary layer within a hurricane's eyewall (Cione et al. 2016, 2020). In addition to the expanding capabilities of small weather-sensing UAS, fleets of commercial drone are also being equipped with sensors for measuring the current atmospheric state to support their operations (e.g., Fleischer 2019). The rapid growth in commercial operations and maturing sensing capabilities can potentially lead to small UAS filling a known data void in the lower atmosphere (e.g., Vömel et al. 2018; Barbieri et al. 2019; Robinson et al. 2020).

While additional work is still needed to move UAS toward full autonomy via reduced cost and increasing reliability, an operational demonstration of the vision laid out by Chilson et al. (2019) to develop a 3D mesonet by coupling automated weather-sensing UAS (including automated recharging) with existing surface-based mesonet stations is nearing fruition (Leuenberger et al. 2020). Concepts for using self-organizing swarms of drones to sample evolving atmospheric features are currently being developed (Hildmann et al. 2019). For example, Reymann et al. (2018) recently demonstrated a UAS capable of sampling the Lagrangian evolution of a trade wind cumulus cloud. These techniques will allow small UAS to autonomously adapt to a range of environmental conditions thus enabling the continuous, simultaneous sampling of submesoscale atmospheric flow features and atmospheric stability that can be assimilated into mesoscale models or used directly by weather forecasters. This paradigm has been demonstrated during a recent field study that used a fleet of small UAS to simultaneously sample low-level winds, moisture and stability to improve supercell thunderstorm predictions (Frew et al. 2020).

Progress will continue in developing both onboard sensor technologies and methods for performing targeted sampling of the lower atmosphere. Combining new sensing strategies (i.e., scheduled and on-demand weather-sensing UAS) with observations collected symbiotically (i.e., not primary mission) during routine commercial UAS flights could provide unprecedented sampling of the lower atmosphere. As their usage expands, the impact of assimilating commercial UAS observations into operational mesoscale models could ultimately rival that which has been demonstrated for observations collected with commercial aircraft via the Aircraft Meteorological Data Relay (AMDAR) program (Cardinali et al. 2003; Benjamin et al. 2010; Petersen 2016; Petersen et al. 2016; James and Benjamin 2017). Petersen et al. (2016) demonstrated the value of a limited number of aircraft moisture measurements as compared with using radiosondes alone.

Observing System Experiments (OSEs) performed by James and Benjamin (2017) indicate that the assimilation of commercial aircraft observations has the single greatest impact on the accuracy of regional mesoscale model prediction among all conventional observing systems and several satellite products (e.g., satellite-derived atmospheric motion vectors, cloud top pressure and temperature, and satellite radiances). In fact, recent sensitivity studies indicated that the substantial reduction in airline operations caused by the COVID-19 pandemic significantly reduced the accuracy of mesoscale predictions of temperature, winds, and humidity by as much as 60% averaged over an entire season (James et al. 2020). Despite the notable gains in skill afforded by commercial airline observations, additional low-level atmospheric observations are needed because commercial aircraft spend little time in the lower atmosphere, and the limited time spent at these low altitudes is constrained to major airport locations. In contrast, small UAS coverage within the lower atmosphere is expected to flourish in the next decade (FAA 2020). The combination of meteorological observations from small commercial UAS and dedicated UAS observing systems would be complimentary to those obtained with commercial aircraft.

In this study, the value of assimilating UAS observations collected during the Lower Atmospheric Process Studies at Elevation—a Remotely piloted Aircraft Team Experiment (LAPSE-RATE) field experiment (de Boer et al. 2020d) is assessed. While previous studies have explored the value of assimilating UAS observations with various assimilation techniques (Jonassen et al. 2012; Ágústsson et al. 2014; Flagg et al. 2018; Sun et al. 2020), to our knowledge, this study represents the first attempt to assimilate observations obtained from a large fleet of UAS using regional ensemble adjustment Kalman filter (EAKF) data assimilation (DA). In this paper, details of the EAKF configuration are given and results for a challenging test case (evolution of terrain-driven flows in complex terrain) are discussed. The test case and observational platforms used in this study are described in section 2. Details of the EAKF data assimilation system and model configuration are described in section 3. The results are presented in sections 4 and 5 followed by a brief discussion of the results and an outlook to the future in sections 6 and 7, respectively.

2. LAPSE-RATE observations

Observations used in this study were collected during the International Society for Atmospheric Research using Remotely Piloted Aircraft (ISARRA) LAPSE-RATE field campaign (de Boer et al. 2020d). It took place in Colorado's San Luis Valley (SLV) in July 2018 with observing systems distributed throughout the northern half of the valley (Fig. 1). The SLV is one of the largest high alpine deserts in the world. It is flanked by the La Garita and San Juan Mountains to the west and the Sangre de Cristo Mountains to the east. Two major canyons spill into the valley from the west with the Saguache

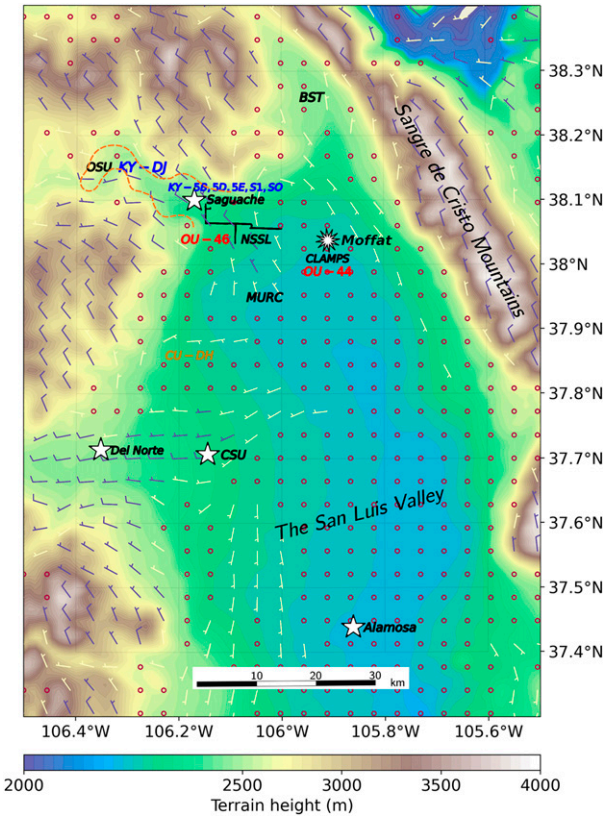

FIG. 1. A bird's-eye view of San Luis Valley showing the platform locations during the drainage flow IOP. The shaded contours show terrain heights, with the San Juan Mountains to the west and the Sangre de Cristo Mountains to the east. Wind barbs (from a deterministic WRF simulation) at 100 m AGL are shown at 1130 UTC and are red, yellow, and blue for <2.5, 2.5–5, and 5–10 m s^{-1}, respectively. Surface station locations are marked with a white star and are discussed in Table 2, and the town of Moffat is marked with a dodecagram. The locations of assimilated UAS observations are labeled in colored text and are discussed in Table 1. Additional observations used for verification are labeled in black text (see Tables 1 and 2). The black line segments to the southeast of Saguache show the UNL CoMet-2 mobile mesonet track. The dashed orange line shows the Saguache canyon.

Canyon entering from the northwest and the Rio Grande River Canyon emanating from the southwest. The two mountain ranges come together at the northern end of the valley with Poncha Pass [2746 m above mean sea level (MSL)] connecting the SLV with the Arkansas River Valley to the north. Conventional observations within the SLV are limited to just a few surface observations, partial coverage with the Pueblo NEXRAD radar and satellite observations.

The SLV experiences a large diurnal cycle in temperature, which is due to a limited amount of moisture, that drives mesoscale and finer-scale flow patterns into and within the valley. These features make the SLV an interesting "laboratory" for testing new atmospheric observing systems and data assimilation techniques targeting improved skill of mesoscale predictions. LAPSE-RATE consisted of daily intensive observation periods (IOPs) in which a number of small UAS were deployed to predefined locations across the northern half of the valley to observe the evolution of the lower atmosphere under a variety of mesoscale forcing conditions. Data collected during the IOP on 19 July 2018 were used to evaluate the utility of UAS observations to improve analysis and prediction of drainage flow evolution using an EAKF data assimilation approach.

a. Drainage flow IOP

Cold air drained from the Saguache canyon (Fig. 1) every morning during LAPSE-RATE (see Pinto et al. 2021). Drainage flows originate from nocturnal radiative cooling in the surrounding higher terrain that generates gravity driven density currents that flow down slopes and canyons (Defant 1951). On 19 July 2018, radiative cooling was fairly strong with the surface air temperature at Saguache Airport dropping a total of 17°C overnight (Fig. 2a). The cooling was interrupted at 0600 UTC as high clouds drifted over the northwestern portion of the SLV during this time. Drainage winds from the northwest occurred throughout the night at Saguache (Fig. 2c). The drainage winds abruptly turned to the up-canyon direction at 1500 UTC (about 3 h after sunrise). The magnitude of the overnight cooling was similar at Moffat (Fig. 2b). At Moffat, low-level winds retrieved with the CU Doppler lidar suddenly shift from west-northwesterly to easterly after 0600 UTC (local midnight) in response to drainage winds down the west side of the Sangre De Cristo Mountains (Fig. 2d). After sunrise, the flow at Moffat trends toward southerly through the morning hours as the flow in the SLV transitions to upvalley. The differences in the evolution of winds at these two sites located just 25 km apart reveals the importance of using a high-resolution model with accurate terrain representation and the accompanying DA with flow-dependent error covariance structures on the scale of the local terrain-driven flows.

During the drainage flow IOP, UAS platforms and mobile mesonets were deployed to Sagauche canyon and to the northwest quadrant of the SLV (Fig. 1; Table 1) to sample the depth, extent, and timing of the drainage flow. Regular UAS flights started at 1130 UTC (0530 MDT), the coldest point of the day, and continued until 1700 UTC, capturing the reversal in flow from drainage to up-canyon and upvalley at 1500 UTC. Multiple radiosondes were launched from both a mobile sounding vehicle at North Farm and from the Collaborative Lower Atmospheric Mobile Profiling System (CLAMPS) at Moffat. Data from all non-UAS observing systems were used to evaluate the simulations.

b. Description of UAS observations

Several universities deployed a mix of UAS platforms (both fixed wing and multirotor) to collect measurements of temperature, humidity and winds within the evolving boundary layer (de Boer et al. 2020c). Details of where and when each of the UAS platforms flew and other characteristics about sampling methods, including the abbreviated labels used in the text and figures, are given in Table 1. In this study, only observations obtained with the University of Colorado Boulder (UCB) DataHawk2 (labeled CU-DH), University of Kentucky

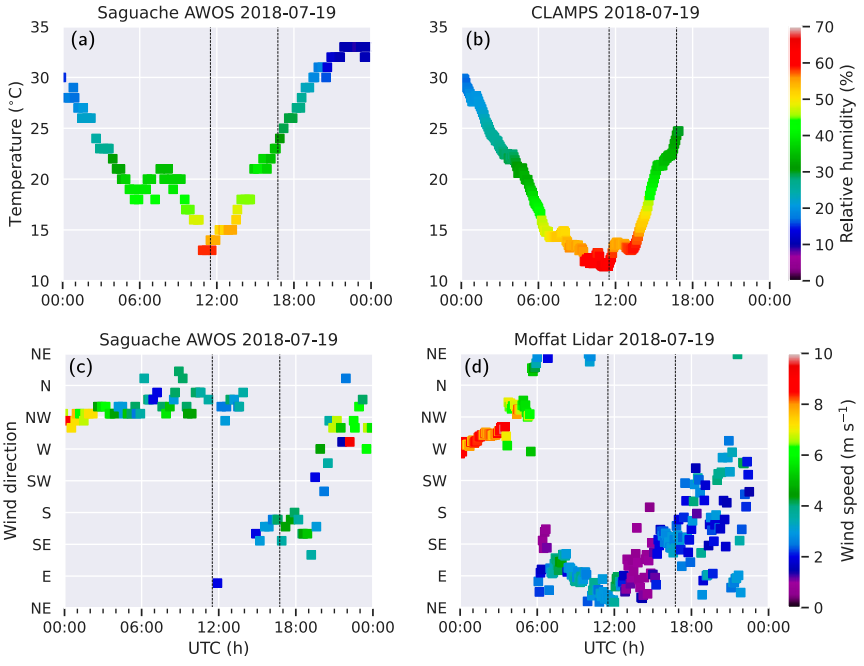

FIG. 2. Observations obtained during the drainage flow IOP including temperature (value on ordinate) and relative humidity (value denoted by the color bar) from (a) the Saguache AWOS and (b) the CLAMPS (located at Moffat). Also shown are wind direction (value on ordinate) and wind speed (value denoted by the color bar) from (c) the Saguache AWOS and (d) the lowest return height (40 m AGL; 1-min averages) of the Windcube lidar at Moffat. The vertical dashed lines indicate the period during which UAS flew.

(UKY) Boundary Layer Unmanned Experiment for the Characterization of Atmospheric Turbulence, generation 5, (BLUECAT5) (labeled KY-5B, KY-5D, and KY-5E), UKY DJI M600P (labeled KY-DJ), UKY SOLOW (labeled KY-SO), UKY S1000 (labeled KY-S1), and University of Oklahoma (OU) Coptersonde 2s (labeled OU-44 and OU-46) were assimilated (de Boer et al. 2021a; Bailey et al. 2020b; Pillar-Little et al. 2021). Data from each of these platforms were obtained from the Zenodo data archive (de Boer et al. 2020b; Bailey et al. 2020a; Greene et al. 2020).

Profiles of temperature and u- and v-wind components of the total wind were obtained continuously at several locations in Saguache Canyon and across the northern portion of the SLV (Fig. 3). Several UKY fixed wing aircraft (KY-5B, KY-5D, and KY-5E) flew stacked north–south transects over Saguache Airport. The KY-DJ flew transects across a narrowing portion of the canyon 6 km to the northwest of the airport. At the same time, OU Coptersonde 2s performed rapid vertical profiling up to 925 m above ground level (AGL) (3225 m MSL) near the mouth of Saguache Canyon and at Moffat. Low-level

TABLE 1. Summary of UAS platforms and locations for the 19 Jul 2018 drainage flow IOP. In the profiling method column, "Step" indicates horizontal transects of the given length with short ascents/descents at the end of each transect to form a raster pattern, "Up/down" indicates a vertical profile straight up and down, and "Spiral" indicates upward and downward spirals with the given radius.

UAS airframe	Operating period (UTC)	Profiling method	Profiling interval (min)	Max height (m AGL)	Mean lat, lon	Legend label
UKY BLUCAT5B	1250–1640	Step: 2.3 km	—	125–200	38.094, −106.164	KY-5B
UKY BLUECAT5D	1200–1640	Step: 3.5 km	—	175–425	38.094, −106.164	KY-5D
UKY BLUECAT5E	1245–1540	Step: 2.1 km	—	150	38.094, −106.164	KY-5E
UKY DJI M600P	1130–1715	Step: 1.3 km	—	270	38.150, −106.272	KY-DJ
UKY S1000	1210–1715	Up/down	60	310	38.094, −106.162	KY-S1
UKY SOLOW	1130–1645	Up/down	2	120	38.094, −106.162	KY-SO
OU Coptersonde 2	1245–1715	Up only	15	925	37.997, −105.912	OU-44
OU Coptersonde 2	1130–1715	Up only	15	925	38.036, −106.113	OU-46
UCB DataHawk2	1430–1815	Spiral: 0.5 km	5	350	37.864, −106.176	CU-DH
OSU SOLO-I	1226–1715	Up/down	10	450	38.036, −106.133	OSU
BST S1	1200–1400	Stepped-Spirals: 0.8 km	10	330	38.266, −105.944	BST

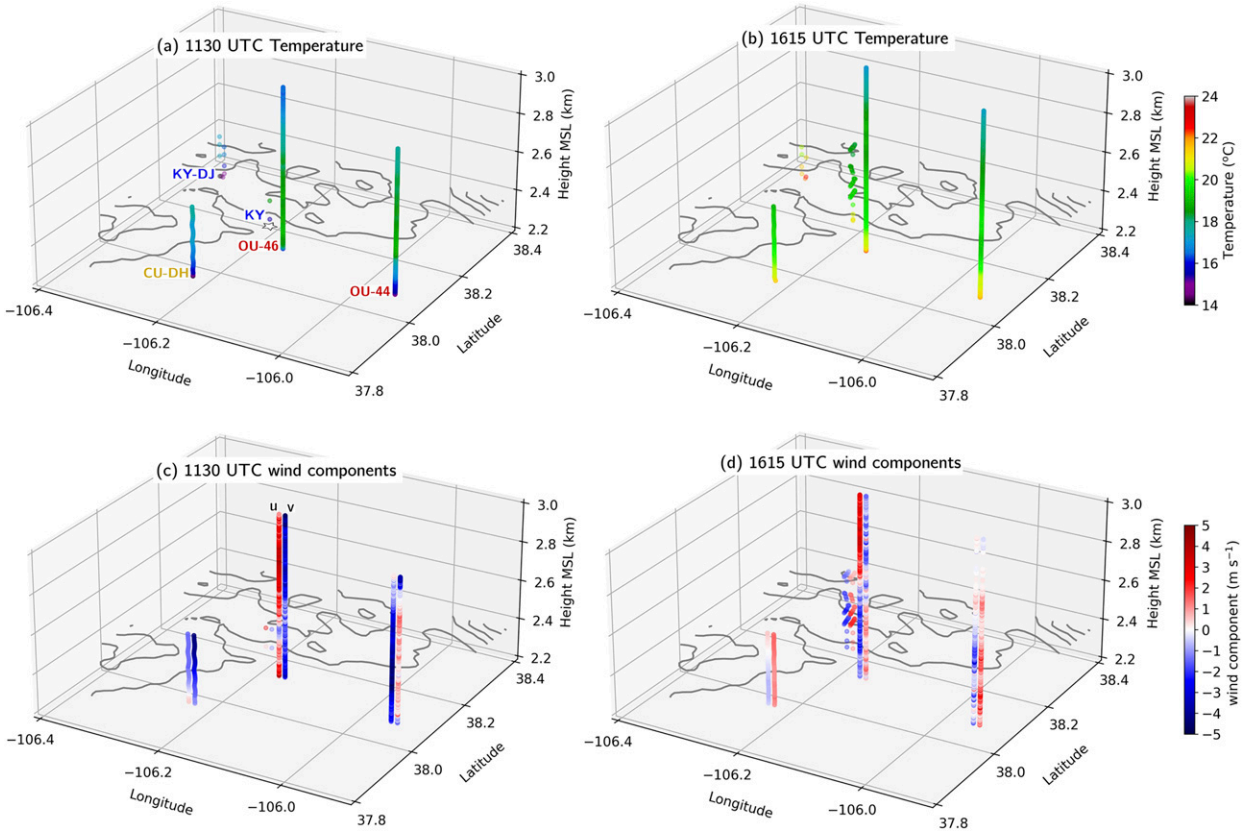

FIG. 3. Profiles of (top) temperature and (bottom) u wind and v wind measured by multiple UAS platforms during the drainage flow IOP at (a),(c) 1130 and (b),(d) 1615 UTC. The u-wind and v-wind components are plotted adjacent to one another in (c) and (d), with u winds to the left. The platforms are labeled in (a), and their locations are shown in Fig. 1. Winds were not measured by the KY-DJ multirotor UAS. Terrain contours (gray lines) are given in 0.5-km increments, with the innermost contour representing 2.5 km MSL. The location of the Saguache AWOS is marked with a white star in (a).

temperature observations indicated the presence of a surface-based inversion at most of the profiling sites (Fig. 3a). The u- and v-wind observations obtained with UAS reveal the spatiotemporal variability of flows across the valley. Prior to sunrise a northerly component is evident on the west side of the SLV and in the canyon while on the east side of the SLV winds are southeasterly through a deep layer (Fig. 3c). By mid-morning, winds shift to more southerly component across all low levels but with northerly winds persisting aloft on the west side of the SLV (Fig. 3d).

Additional UAS observations were obtained outside the area shown in Fig. 3, including those obtained with the Oklahoma State University (OSU) SOLO-I (Jacob et al. 2020; farther up Saguache Canyon) and Black Swift Technologies (BST) S1 (Elston and Stachura 2020; located south of Poncha Pass). Observations from these UAS were used to evaluate the drainage flow case DA experiments.

Data quality considerations are an important aspect of data assimilation. For example, data obtained during the rapid descent phase of the OU Coptersonde 2 profiling were omitted from the final observational data stream because the descent rate exceeded the time constant of the TRH sensor (Pillar-Little et al. 2021). These observations were removed during quality control procedures applied during postprocessing by the UAS operators and thus, were not available for assimilation. Observations obtained from other UAS profile descents were assimilated. Temperatures measured by the UCB DataHawk2s were 1.2°C higher than measured by the Mobile UAS Research Collaboratory (MURC) tower, and a correction was made to the final dataset. At the same time, obtaining wind measurements with UAS can also be challenging. Bailey et al. (2020b) reported a low bias in wind speed of roughly 25%. In addition, Bell et al. (2021) found that the Coptersonde 2 winds had a systematic low bias of about 1 m s^{-1} that they hypothesized was due to the nonlinear relationship between pitch required to maintain profile location and drag associated with the changing form factor of the tilting aircraft. They also showed that correlations between UAS wind direction and those obtained with radiosonde and the CLAMPS lidar where much lower than those found for wind speed. Despite these issues, Barbieri et al. (2019) found that observations obtained by a range of UAS deployed during LAPSE-RATE agreed remarkably well (particularly for temperature) with wind measurements having the largest uncertainty (±33%) relative to observations obtained with the MURC tower.

TABLE 2. Summary of other meteorological observations used in this study. Here PTRH/U indicates pressure, temperature, relative humidity, and wind.

Station identifier	Location	Station type	Elev (m MSL)	Lat, lon	Raw data frequency (s)	PTRH/U height (m)
KALS	Alamosa	ASOS	2298	37.435, −105.867	60	2/10
K04V	Saguache Airport	AWOS IIIP	2393	38.097, −106.169	1200	2/10
KRCV	Del Norte	AWOS IIIP/T	2425	37.714, −106.352	1200	2/10
CTR01	Center	CSU CoAgMet	2348	37.707, −106.144	3600	2
MURC	North Farm	CU tower	2325	37.951, −106.033	<1	18
CLAMPS-1	Moffat	Surface station	2305	37.998, −105.912	1	3/—
CoMet-2	Mobile	UNL mobile mesonet	2313–2354	37.893, −105.716	1	2.5/3.25
CU	Saguache Airport	Windcube Doppler lidar	2393	38.907, −106.169	1	40–220
CU	Moffat	Windcube Doppler lidar	2305	37.998, −105.912	1	40–220
CLAMPS-1	Moffat	Lidar wind profiler	2305	37.998, −105.912	1	15–2000
CLAMPS-1	Moffat	Radiosondes	2305	37.998, −105.912	<1	Sounding
NSSL	North Farm	Radiosondes	2313	38.053, −106.051	<1	Sounding

c. *Ancillary observation used for verification*

Four surface meteorological stations are located in the SLV. Three surface stations are located at airports/airfields: KALS (Alamosa), K04V (Saguache), and KRCV (Del Norte), and one, the CSU CoAgMet mesonet station, is located at Center, Colorado (Table 2 and Fig. 1). As part of LAPSE-RATE, Saguache Municipal Airport and Moffat Consolidated School hosted additional observing systems. A detailed description of the observing systems deployed to these sites is given by de Boer et al. (2020d) and summarized in Table 2. Datasets used to evaluate the data assimilation experiments include those collected with the University of Nebraska–Lincoln (UNL) mobile mesonet (Houston and Erwin 2020), the NSSL mobile sounding system (Waugh 2020a), the University of Oklahoma/NSSL Collaborative Lower Atmospheric Mobile Profiling System (CLAMPS) sounding system (de Boer et al. 2021b; Waugh 2020b), two Leosphere WindCube V1 Doppler lidars (Bell et al. 2020b; Lundquist et al. 2020), the MURC (de Boer et al. 2020a) and the CLAMPS Doppler lidar (Bell et al. 2020a; Bell and Klein 2020). Note that the WindCube Doppler lidars retrieve wind profiles with 20-m resolution with range gates between 40 and 200 m AGL, with each profile height being a 20-m average centered at the height. In most cases, only data up to 160 m AGL were reported because of low signal to noise above this height. The higher-powered CLAMPS lidar provides coverage between 100 and 2000 m AGL.

3. Ensemble data assimilation

The impact of UAS observations on analyses and short forecasts is assessed using EAKF data assimilation. This impact is assessed by evaluating both the priors and the posteriors obtained as part of each assimilation cycle as well as a 4-h-long free forecast initialized from the ensemble mean analysis. Ensemble data assimilation was chosen over variational methods to capture uncertainty in the analyses that can be a function of terrain, time-of-day, and flow characteristics (Romine et al. 2013; Ha and Snyder 2014). The representation of uncertainty becomes increasingly critical when attempting to represent the state of the atmosphere at increasingly higher resolution (Brousseau et al. 2012; Schwartz et al. 2019). EAKF also allows for the representation of uncertainties in the UAS measurements, which determines the degree to which the analyses are fit to the observations. As such, the ensemble Kalman filter framework is well suited for quantifying these uncertainties while at the same time being able to optimally incorporate a range of observational datasets with known or estimated error characteristics.

a. *DART*

The data assimilation experiments were run using the Manhattan release of NCAR's Data Assimilation Research Testbed (DART; Anderson et al. 2009). DART uses an ensemble adjustment Kalman filter (Anderson 2001) that draws the model state toward being more consistent with observations while taking into account observation error. After the filter runs, the ensemble of new model states are integrated forward in time, and then these steps are repeated sequentially (cycled). DART was cycled every 15 min to allow the system to take full advantage of the frequently updating distributed network of UAS observations. The EAKF (Anderson 2001) was configured to use 40 ensemble members with posterior inflation (relaxation to prior spread) and sampling error correction (Anderson 2012; Necker et al. 2020). Posterior inflation is time invariant with a value of 1.12 to maintain ensemble spread in the response to the relatively dense collection of UAS observations that can act to reduce the ensemble spread.

Vertical and horizontal filter localization values were used to prevent observations from impacting unrelated state variables that may be spuriously correlated at sufficiently far distances from an observation. Both 333-m and 1-km vertical localization values were tested, which are roughly equal to one-third and the entire profiling depth of the highest-flying (OU) platforms, respectively. Both vertical localization values produced similar results, with the 333-m value being slightly more skillful in predicting the shallow drainage flow observed at Saguache Airport.

Assimilation results are also very sensitive to the horizontal localization value (Sobash and Stensrud 2013). Results from sensitivity simulations (not shown) were used to explore the

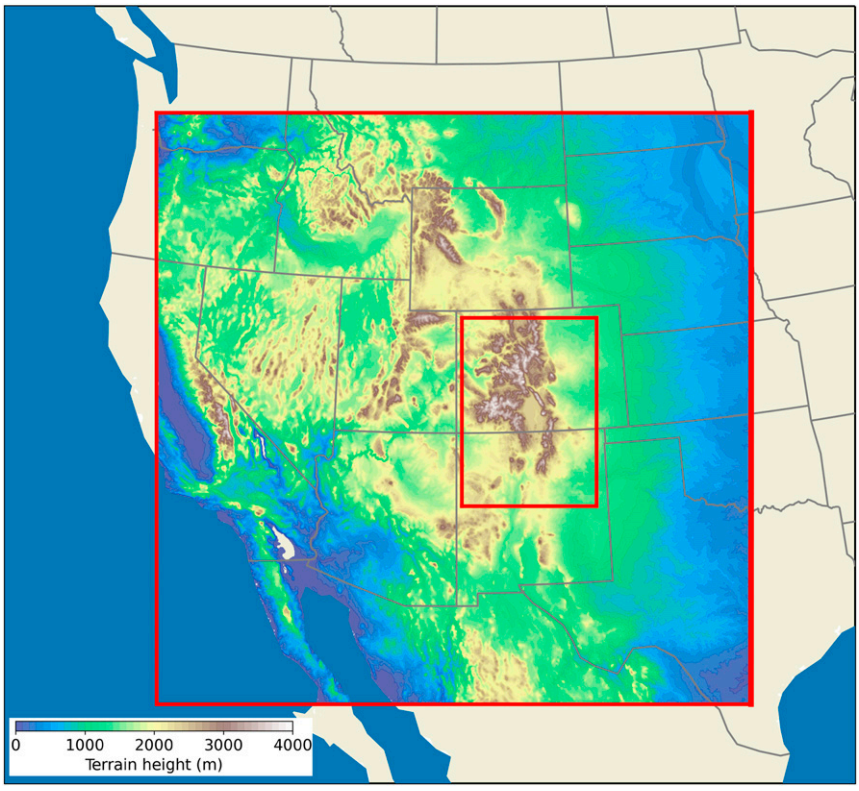

FIG. 4. The two WRF domains are outlined in red. The outer domain (d01) and inner domain (d02) used grid spacings of 3 and 1 km, respectively; DA was performed on d02 only. The color contours indicate the terrain height from d01.

impact of horizontal localization on forecasts valid at Saguache. Based on these sensitivity experiments it was decided to use a horizontal localization value (the maximum horizontal distance that an observation can have an impact) for UAS observations of 127 km. This value was determined based on the spacing between UAS profiling sites and the size of the SLV. A more detailed evaluation of the impact of the localization values for operational UAS observations is beyond the scope of this study, but is something to consider in conjunction with the design of operational networks of UAS observing systems (Chilson et al. 2019). Future work is needed to more fully assess localization choices for a range of environments and sampling strategies. For the purposes of demonstrating the value of UAS observations for short-term, low-level wind predictions, only the results using the 333-m vertical and 127-km horizontal localization values for UAS observations are discussed below.

b. *WRF Model*

The Weather Research and Forecasting (WRF) Model (Skamarock et al. 2008; Powers et al. 2017), version 3.9.1.1, was used to integrate the ensemble members forward in time. WRF is a nonhydrostatic, compressible model that uses a hybrid terrain-following coordinate system. A one-way nested configuration (Fig. 4) was used to drive the innermost 1-km domain. Observations were only assimilated within this innermost domain. The outer domain was configured to capture the larger-scale upstream flow features that influenced the region of interest during LAPSE-RATE. Both domains used 45 vertical levels from the surface to 200 hPa. Since the focus of this study was to assess the performance of the model at predicting low-level flow features in complex terrain, the hybrid coordinate system was stretched in order to maximize vertical resolution (nominally 50 m) in the lowest 1 km of the atmosphere with the lowest model level being at approximately 13 m AGL. Both domains used a 4-s time step. The physics parameterizations used were the MYNN PBL scheme (Nakanishi and Niino 2009), the RRTMG longwave and shortwave radiation schemes (Mlawer et al. 1997; Iacono et al. 2008), the Noah LSM (Chen et al. 1996), and WSM6 microphysics (Hong and Lim 2006). High, thin clouds were present both in the observations and the model during overnight hours that likely influenced the evolution of the drainage flow. Preliminary sensitivity studies indicate that these results are not very sensitive to the choice of microphysics scheme at the short lead times (<3 h) of interest here. In addition, the ensemble spread adequately spans the range of uncertainty that may be associated with the treatment of cloud microphysics, thus, further exploration of the role of cloud microphysics is beyond the scope of this paper.

1) MODEL INITIAL CONDITIONS

Forty d01 (3-km grid spacing) ensemble members were initialized using the 0400 UTC (19 July 2018) analysis from the

NCEP High-Resolution Rapid Refresh (HRRR; Benjamin et al. 2016). Balanced potential temperature, u-wind, v-wind, water vapor mixing ratio, and pressure perturbations were created for these ensemble members using generic background error statistics (WRFDA CV3; Parrish and Derber 1992). These perturbations were used to generate 40 ensemble members from a single CONUS-scale mesoscale analysis. The lowest model-level temperature and humidity initial perturbations were added to the soil layer values using a method similar to Benjamin et al. (2016). This was done to prevent the loss of ensemble spread in low-level temperature and moisture after the spinup period. The temperature perturbation was added to the 4 soil layers with the magnitude of the perturbation decreasing with depth into the soil using multiplicative factors from top to bottom of 1, 0.6, 0.4 and 0.2. The moisture perturbation was added to the 4 soils layers using constant multiplicative factor of 0.2. Perturbation impacts were constrained as follows for all ensemble members: water vapor mixing ratio was kept above 0.001 g kg^{-1}, soil temperature was kept above freezing and soil moisture volume (unitless) was kept between 0.01 and 1. The d01 ensemble-member initial conditions were interpolated to the 1-km domain (d02). The two domains were then spun up until the first observations were available at 1130 UTC.

2) Model lateral boundary conditions

The d01 (3-km domain) lateral boundaries were forced using the hourly forecast output from the 0400 UTC HRRR run. A unique perturbation field was added to each lateral boundary condition file for the 40 ensemble members. The HRRR forcing was then interpolated to a 15-min interval to support the 15-min data assimilation windows. Boundary conditions for d02 (1-km domain) came from d01 (the 3-km parent domain).

c. Assimilated observations

Observations of temperature, relative humidity and u and v winds (see Fig. 3) obtained from multiple UAS were assimilated. Data from all UAS with a 5-character identifier (UU-xx) listed in Table 1 were assimilated. UKY flight data transects and profiles were postprocessed to 100-m spacing in the horizontal and 10-m spacing in the vertical directions to better match the grid spacing of the model. The UCB Datahawk2 spirals, which took place within a tight 0.5-km radius spiral were averaged in 10-m vertical increments to create profiles. ''Superobs'' were created from all assimilated UAS observations using a horizontal radius of 2 km and a vertical pressure radius of 3 hPa. Superobs are created to reduce the data density, which minimizes the effect of correlated error in the measurements while at the same time reducing the uncorrelated error through averaging (Duan et al. 2018). The technique used to perform superobbing is similar to that described in Torn and Hakim (2008), where all available observations (and their observation errors) of a specific type within some volume are averaged on a coarser grid than is used in the model. Observation error variances for UAS observations were set to constant values, based roughly on the intercomparison assessment reported by Barbieri et al. (2019). The values used for the temperature, relative humidity, and u- and v-wind components observation-error variances were $(1\,\mathrm{K})^2$, $(3\%)^2$, and $(1\,\mathrm{m\,s^{-1}})^2$, respectively. These values are similar to those used previously in EnKF assimilation of observations obtained by commercial aircraft (Dirren et al. 2007).

d. DA experiments

Several experiments were run to evaluate the impact of UAS data assimilation on the evolution of the drainage flow and its transition to upvalley flow. A baseline simulation was performed in which the EAKF DA system was cycled every 15 min but no observations were assimilated (NoDA). A second simulation was performed in which UAS data from multiple platforms were assimilated using 15-min cycling (UAS). The resulting analyses and short-term forecasts obtained with these two configurations are compared to assess the change in skill afforded by UAS. Last, an additional DA experiment is performed in which only surface stations observations (SFC) are assimilated to demonstrate a potential benefit of high-density observations allowing for a reduction of localization scale. Additional observations, including those from NWS radiosondes (Denver International Airport and Grand Junction Regional Airport are the closest to Saguache, 235 km away), commercial aircraft, radar and satellites are not expected to directly influence the low-level drainage flow near Saguache or the low-level temperature, moisture, and winds within the SLV on the short-prediction time scales being considered for the mesogamma-scale event studied here. Thus, for simplicity, surface observations are the only conventional observation type considered. For the SFC experiment, error variances of $(1.5\,\mathrm{K})^2$, $(5\%)^2$, $(1.5\,\mathrm{m\,s^{-1}})^2$ were used following the optimization efforts of Ha and Snyder (2014). Vertical and horizontal localization values of 1 and 382 km, respectively, were used to spread the surface observations. The impact of assimilating UAS observations in addition to surface observations on the accuracy of both the analyses and forecasts will be explored in future work.

4. The impact of UAS observations on simulated terrain-driven flows

a. Assimilation assessment at Saguache

Drainage winds, also referred to as downvalley or mountain winds, and upvalley wind, also referred to as valley winds, are small-scale, buoyantly driven, shallow and often intermittent flows (Defant 1951; Orville 1964; Whiteman 2000). These diurnally driven flow patterns, well known to any canyon-bound road cyclist who often will complain of ''headwinds both ways,'' occur regularly in regions of sloped terrain where radiative cooling at night produces more dense air adjacent to the surface that is forced down terrain gradients via gravity. The resulting drainage flows can contribute to the development of deep cold pools in mountain valleys in which strong stable stratification causes pollutants to build up over time (e.g., Neff and King 1989; Doran et al. 2002). Alternatively, these flows can help to purge pollutants by draining polluted air away from a population center at night (Banta et al. 1997; Pinto et al. 2006). Daytime surface heating along elevated terrain causes a pressure gradient reversal that drives upvalley and up-canyon flows (Rampanelli et al. 2004).

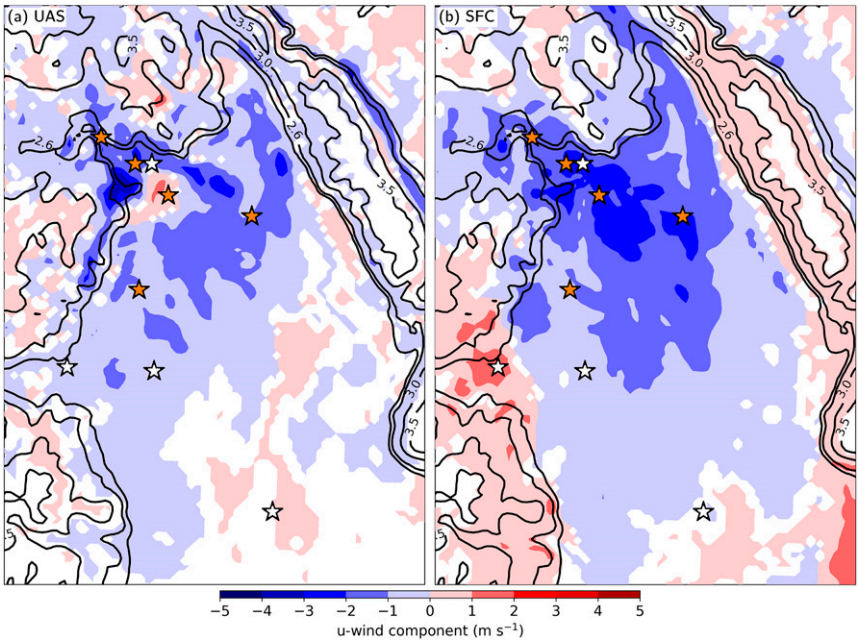

FIG. 5. The analysis increment for the 10-m u-wind component at 1130 UTC obtained for (a) the UAS simulation and (b) the SFC simulation. The orange stars show the locations of assimilated UAS observations that are only assimilated in (a), and the white stars show the locations of assimilated surface observations that are only assimilated in (b). Labeled line contours are terrain heights (km MSL).

Motivated by the need to improve the prediction of this circulation pattern and associated potential impacts, these diurnally varying terrain-driven circulations have been studied for many years (Ives 1939; Defant 1951; Bergen 1969); however, only limited efforts have focused on the impact of data assimilation to improve model skill at predicting these phenomena (e.g., Hacker et al. 2018). The timing and vertical wind structure associated with the transition from drainage to up-valley flow are difficult to analyze and predict in data sparse regions such as the SLV and thus provide a good test of a data assimilation system's ability to capture a mesogamma-scale variability in the wind field.

The impact of the UAS observations is demonstrated by the analysis increment field for the u-wind component (Fig. 5). The analysis increment, plotted for the first cycle when UAS observations are first assimilated at 1130 UTC, reveals that both UAS and SFC DA reduce the strength of drainage winds in Saguache Canyon. However, the analysis increment obtained with UAS DA for the 10-m u-wind field shows much more structure with a narrow ribbon of reduced winds extending into the SLV. The analysis increment obtained for the SFC DA experiment indicates much more widespread reduction in the westerly winds across the northern half of the SLV (Fig. 5b). The analysis increment obtained with UAS DA is consistent with wind observations obtained with the UKY BLUECAT5 transects that indicated that the strongest drainage winds occurred to the south of Sagauche Airfield (Bailey et al. 2020b)—note the localized area of enhance westerlies in Fig. 5a.

Results from NoDA and UAS DA are compared to fully understand the direct impact of UAS DA on the predicted evolution of conditions at Saguache Airfield using independent observations from the Saguache Automated Weather Observing System (AWOS) for verification. Time series of successive 15-min forecasts (ensemble mean and spread) of surface meteorological variables obtained for the NoDA and UAS DA experiments are shown in Fig. 6. The UAS DA reduces analysis uncertainty while increasing the accuracy of the 15-min forecasts of 2-m temperature and relative humidity. The NoDA experiment has persistent warm and dry biases that are decreased by 38% and 82%, respectively, in the UAS DA simulation. In addition, UAS DA clearly reduces model spread in both 2-m temperature and relative humidity while still capturing the observations within the $\pm 2\sigma$ spread. The RMSE values are reduced as well, indicating a more accurate depiction of the transition from a cool, moist stable surface layer to a warm and dry convective surface layer.

UAS DA, which begins at 1130 UTC, attempts to reduce the u-wind bias, but not by much, owing to this level of variability occurring at a finer scale than can be resolved by the model. Nonetheless, the overall evolution of the drainage flow and its transition to up-canyon is better captured in the UAS DA experiment. In fact, UAS DA results in smaller biases and a reduction in RMSE in both components of over 30%. While the NoDA simulations struggle to indicate a wind reversal from drainage to up-canyon, UAS DA captures this evolution and even pinpoints the timing of the wind shift occurring at 1430 UTC.

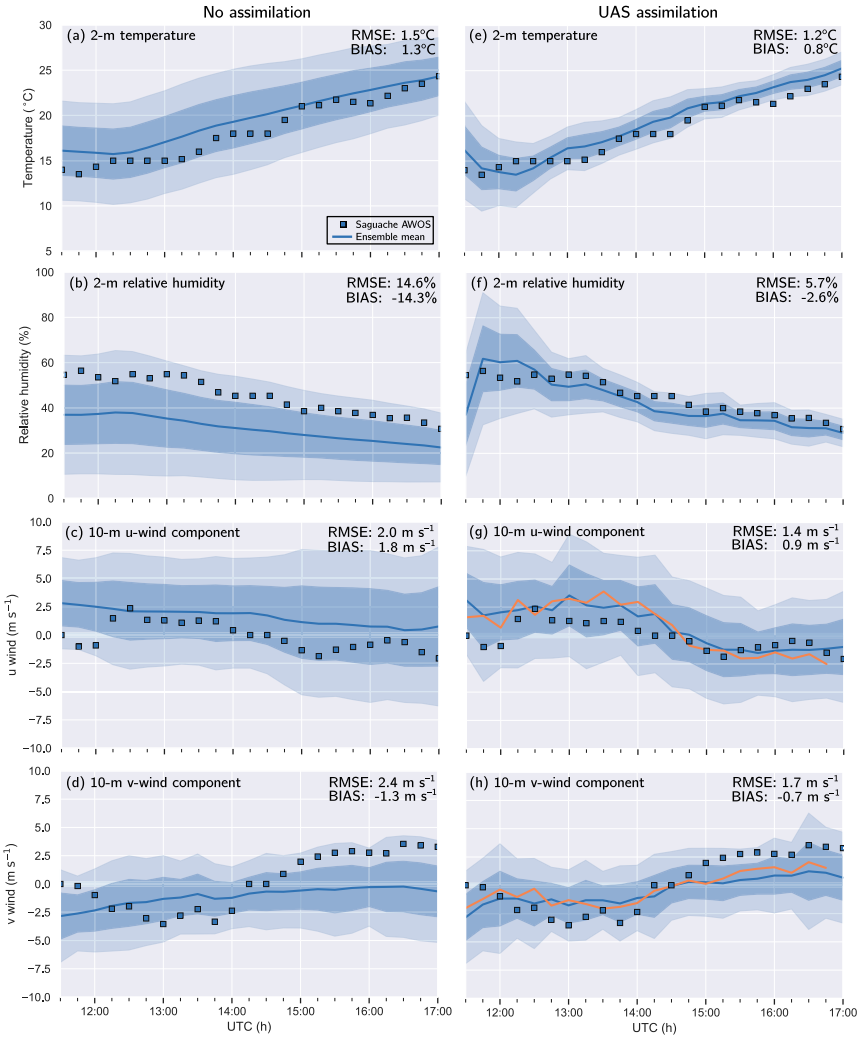

FIG. 6. Time series of ensemble mean of the priors (solid blue lines) for (top) 2-m temperature, (top middle) 2-m relative humidity, (bottom middle) 10-m u-wind component, and (bottom) 10-m v-wind component at Saguache with (a)–(d) no data assimilation and with (e)–(h) UAS data assimilation obtained from successive 15-min cycles. The dark- and light-blue shaded regions show 1 and 2 standard deviations. Data from the Saguache AWOS are shown as the blue squares, and the wind-component analyses at Saguache are shown as the orange lines in (g) and (h). Bias is computed as ensemble mean minus observation.

It can help to better understand some of the remaining biases in the 15-min wind forecasts of the UAS DA experiment by looking at the 10-m wind components obtained from the analyses. Successive analyses of the 10-m u- and v-wind from the UAS DA experiment are shown in Figs. 6g and 6h. Recall that the analyses include the impact of UAS observations that were available within a 15-min window centered on the valid time. The magnitude of 10-m u-wind (i.e., $|u|$) in both the forecasts and analyses tends to be greater than that obtained by the AWOS while the magnitude of the v-component forecast and analysis values (i.e., $|v|$) tends to be smaller than the AWOS values.

This consistent pattern of differences between the DA values (priors and analyses) and the 10-m wind AWOS observations could have resulted from biases in the UAS wind observations. The u-wind values obtained with the fixed-wing UAS (KY-5D and KY-5E) between 20 and 60 m AGL agree fairly well with the UCB Doppler lidar winds in the first range gate at 40 m AGL (Fig. 7). The winds obtained with the KY-SO quadcopter tended to be weaker than the fixed-wing measurements despite already being corrected for a low bias (Bailey et al. 2020b). Nonetheless, all UAS measurements of u wind in this layer indicated a larger u-wind magnitude (e.g., 3–5.5 m s^{-1} at 1230 UTC) than that observed at 10 m by the AWOS (1.5–2.5 m s^{-1}, Fig. 6g). At the same time, the magnitude of the northerly v-component measured by the UAS (2–3.5 m s^{-1}) was similar to that obtained by AWOS. The assimilation of these larger UAS u-wind values at model levels

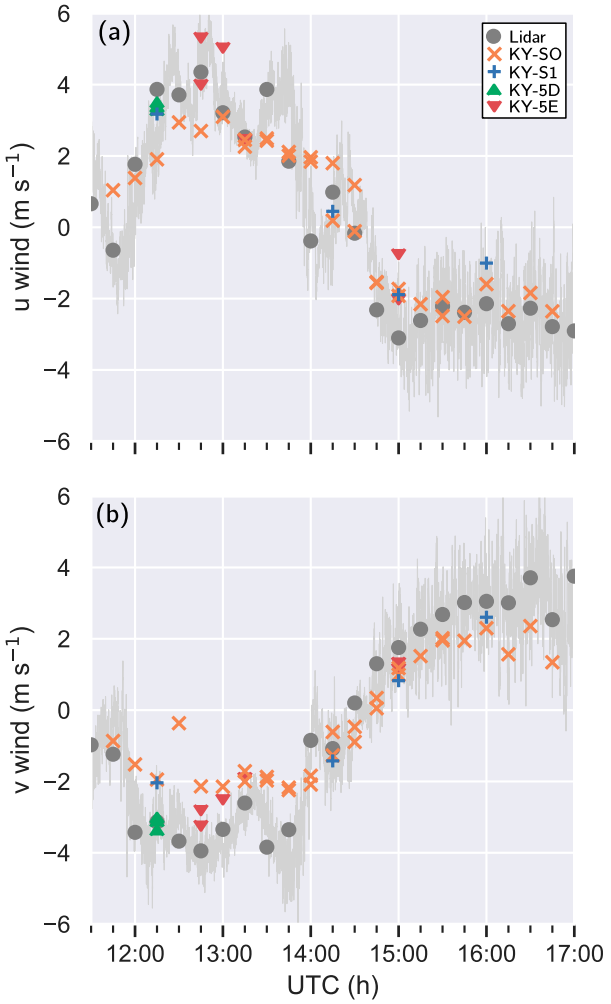

FIG. 7. Time series of (a) u-wind component and (b) v-wind component from the lowest return height of the Doppler lidar (40 m AGL) and averaged for 60 s (gray line). Also shown are the 15-min-averaged lidar observations (gray circles) and the assimilated UAS observations from approximately 20–60 m AGL obtained from several UKY UAS (KY-SO and KY-S1 are multirotor and KY-5D and KY-5E are fixed wing UAS) that were flown at Saguache Airport (orange, blue, green, and red symbols).

between 20 and 60 m AGL tended to drive the simulated u winds away from the weaker AWOS values. A similar, but opposite effect is evident during up-canyon flow. During the up-canyon winds that occurred after 1430 UTC, the magnitude of the v-wind component obtained with all of the UAS (and KY-SO in particular) tends to be smaller than that observed with the lidar (Fig. 7b). This systematic underestimate of the magnitude of the v-wind component results in the v-wind analyses at 10 m being too weak after 1500 UTC (Fig. 6h). This detailed assessment demonstrates the sensitivity of DA to observational biases and the importance of continuing to improve wind measurements obtained by small UAS, particularly in weaker wind regimes. At the same time, the EnKF DA can be improved either by including vertically varying or environmentally dependent observation error covariances. That is, the UAS wind error covariances could be made to be a function of the wind speed. Last, new techniques that are being developed to explore ways of implementing dynamic localization could be employed so that the size of spatial filter is a function of environmental conditions (e.g., Lei et al. 2020).

To explore the impact of UAS DA on the vertical structure of winds at Saguache, the 15-min forecasts of the ensemble mean wind components from the NoDA and UAS DA experiments are compared with winds obtained with the CU Doppler lidar (Fig. 8). The 1-s lidar data are averaged to 15 min and linearly interpolated in height to match the model vertical levels. The model vertical grid spacing at low levels is such that the lidar return heights are within 9 m of the grid levels.

The 15-min lidar observations (Fig. 8a) reveal a rapidly evolving drainage flow with an initially elevated core that descends toward the surface before dissipating between 1400 and 1500 UTC. The ensemble mean winds from the NoDA simulation indicate the presence of a strong drainage flow with an elevated core of stronger winds that decreases linearly in time. Consistent with comparisons with surface observations (Fig. 6), the time–height cross sections of ensemble mean winds obtained with 15-min cycles in NoDA show no indication of shift to upvalley flow (Fig. 8b). The 15-min ensemble mean forecasts of winds obtained with UAS DA do a better job of capturing the observed descent of the drainage flow jet toward the surface and reversal of winds to up-canyon just after 1430 UTC (Fig. 8c), which never occurs in the NoDA simulation. While the upvalley flow obtained with UAS DA is weaker than observed, this may be due, in part, to biases in the UAS wind component measurements relative to those obtained with the Doppler lidar, as noted above. Nonetheless, the u-wind and v-wind biases averaged over all lidar return heights and times are reduced by roughly 40% when UAS observations are assimilated. At the same time, UAS DA reduces the RMSE in low-level u- and v-wind components by over 40% by providing a better representation of the decent of the low-level jet core and timing of the flow reversal.

Vertical profiles of state-space RMSE are shown for both analyses (after assimilation) versus and the forecasts (priors) for temperature, relative humidity, and both wind components (Fig. 9). The RMSEs are computed by differencing the model values (priors and analyses) from the superobbed UAS observations that have been interpolated into model space. The RMSE represents an average across the entire domain for all 15-min DA windows for each 10-hPa layer. While differences in mean errors of the temperature forecasts and analyses are relatively small, these differences are much larger for relative humidity and the wind components. Smaller RMSEs are found for relative humidity with the maximum difference being near the surface. The wind-component RMSEs, which peak at 2 m s^{-1} for the u-wind forecasts are reduced to 0.5 m s^{-1} for both components after assimilation (Fig. 9b). These plots indicate that UAS data are clearly having a positive impact on winds and relative humidity within the lowest 1 km of the atmosphere.

b. *Assimilation assessment across the San Luis Valley*

The impact of UAS data assimilation is also assessed using independent NSSL and CLAMPS radiosonde data obtained at

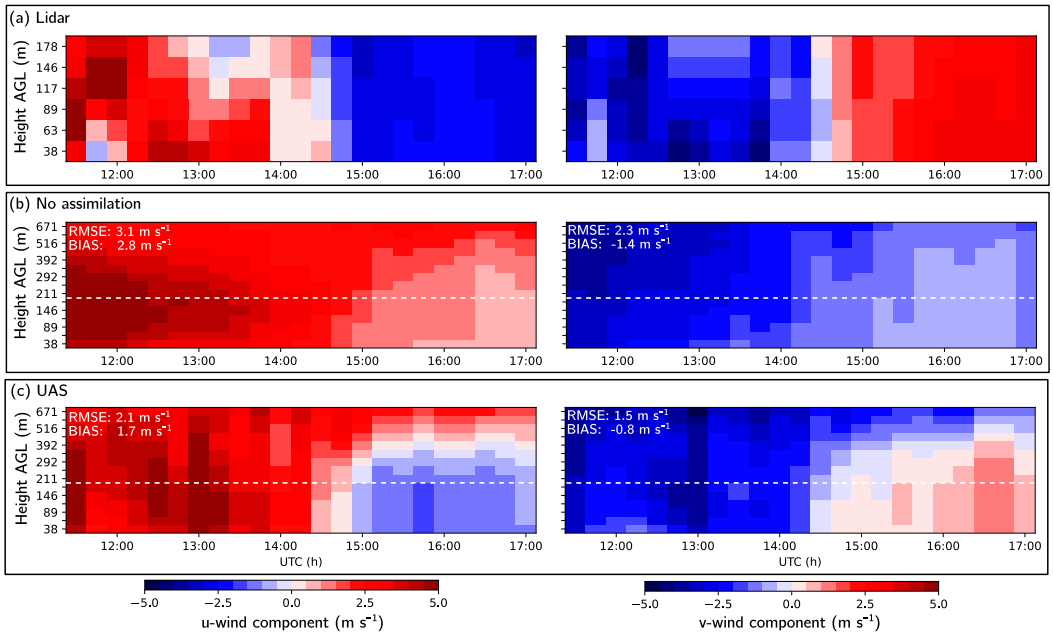

FIG. 8. Time–height plots of (left) u-wind component and (right) v-wind component at Saguache Airport from (a) the Doppler lidar, (b) priors from no assimilation, and (c) priors from UAS assimilation. The dashed white lines in (b) and (c) show the approximate maximum vertical range of the lidar shown in (a). Bias and RMSE computed across all range gates and times shown.

two locations in the SLV separated by 15 km (see Fig. 1). The NSSL sounding at 1300 UTC shows evidence of a shallow layer of very light drainage winds (northwesterly) from the surface up to 100 m, southeasterlies from 100 to 500 m and northwesterlies aloft (Fig. 10). The sounding data are only plotted at model vertical levels to facilitate direct comparison with the ensemble mean 15-min forecasts. While neither simulation is able to capture the fine-scale variations in vertical structure that were observed at this time, the UAS DA clearly shifts the profile closer to reality than the NoDA benchmark. The biases in each component are reduced by over 30%. In addition, the uncertainty (given by the ensemble spread) in the UAS run is clearly reduced compared to the NoDA simulation while, impressively, the observed values still fall within 1σ of the ensemble mean. Note that the simulated vertical variations are smoother than observed, likely because of excessive vertical diffusion by the PBL scheme and perhaps also ensemble averaging.

The 1300 UTC CLAMPS radiosonde observations indicate the presence of a easterly jet at 325 m shifting to northwesterly above 750 m with lighter southeasterly winds just above the surface (Fig. 11). The NoDA experiment ensemble mean indicates northwesterlies from the surface to 1 km AGL with no indication of a jet core, completely missing all aspects of the observed vertical variations in winds. In contrast, the UAS DA experiment ensemble mean captures the low-level easterly u-wind component with a weak enhancement of the easterly winds at 325 m. While still underestimating the strength of this easterly jet, the overall representation of u winds results in significant reductions in u-wind RMSE and bias relative to NoDA. These improvements come at the expense of a slight degradation in the v-wind component in the UAS DA experiment due to increased offsets in the representation of the v wind just above the surface (manifested as an erroneous northerly component between the surface and 250 m). It is hypothesized that the smoother jet structure in the UAS DA may be the result of averaging among all members, but, again, may also have been caused by excessive vertical diffusion of momentum by the PBL scheme. Additional studies using meso- to microscale coupling experiments are being performed to evaluate the role of the PBL scheme in underestimating the strength of the easterly jet in this case.

A comparison of the modeled and observed temperature and humidity profiles at the NSSL sounding location is shown in Fig. 12. Both simulations struggle with the inversion strength (5°C) and/or depth. The 10 m depth of the inversion cannot be captured by either simulation because the model vertical resolution is too coarse. The UAS DA simulation captures the magnitude of the temperature inversion (5°C) much better than NoDA. While the NoDA simulation has a smaller RMSE for temperature, it underpredicts the strength of the surface-based inversion by a factor of two and has very large uncertainty. The UAS DA reduces uncertainty by a factor of 2 while still bracketing the truth, albeit with uncertainty approaching 2σ just above the surface. Similar to issues with capturing fine-scale vertical variation in the wind, the layer of cold temperature biases below 325 m is likely, in part, due to issues with handling vertical mixing by the PBL scheme under strongly stable conditions (e.g., Shin and Hong 2011; Dimitrova et al. 2014) and points to the need for further investigation of the coupling between high-resolution DA and PBL scheme response. The temperature profile obtained with UAS DA

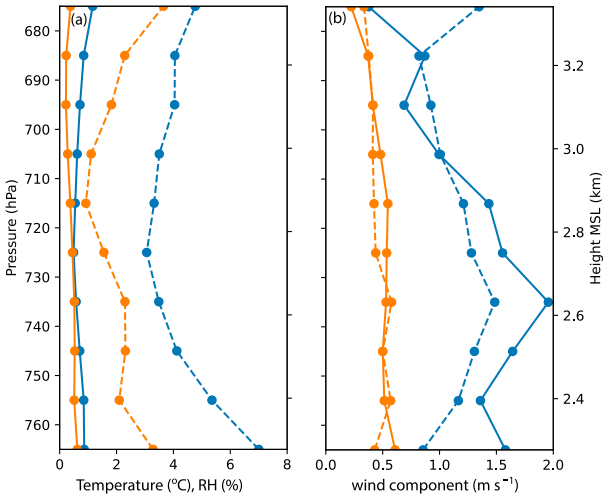

FIG. 9. Domain- and time-averaged state-space RMSE at 10 interpolated levels (obtained by averaging all comparisons within each 10-hPa vertical slice) as computed by comparing the forecast priors (blue) and analyses (orange) with UAS observations (interpolated in model grid space) for (a) temperature (solid) and relative humidity (dashed), and (b) u wind (solid) and v wind (dashed). A total of 1505 temperature and relative humidity observations (after superobbing) were assimilated and 1365 u- and v-wind observations were assimilated over the period from 1130 to 1645 UTC.

captures the 500-m vertical extent of the observed isothermal layer while the NoDA experiment is essentially adiabatic above 125 m.

Improvements are also evident in the analyses of relative humidity. UAS DA greatly reduces the dry bias evident in the

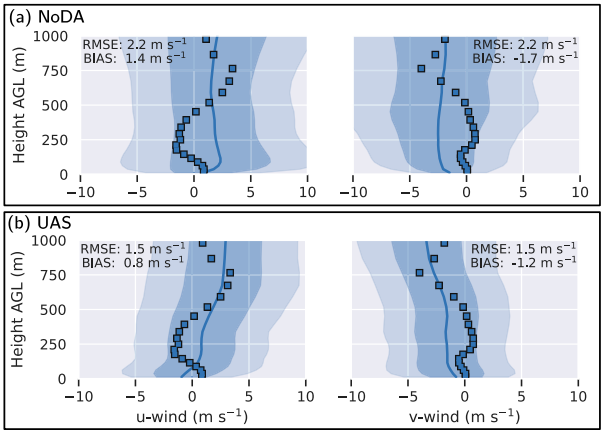

FIG. 10. Profiles of (left) u-wind component and (right) v-wind component given by the ensemble mean of priors (solid blue lines) valid at 1300 UTC for (a) no assimilation and (b) UAS assimilation for the grid point nearest to the NSSL radiosonde launch location. The dark- and light-blue shaded regions show 1 and 2 standard deviations. The sounding wind components interpolated to model levels are given by the blue squares. The RMSE and bias are given for this single comparison time.

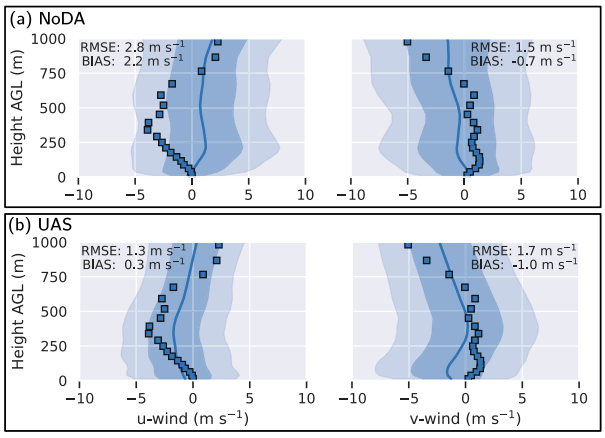

FIG. 11. As in Fig. 10, but for the grid point nearest the CLAMPS and observations from radiosondes launched at the CLAMPS location.

NoDA simulation and picks up on the magnitude of the low-level moisture inversion that is completely missed in the NoDA simulation. In fact, the dry bias in the ensemble mean of the NoDA experiment of over −30% near the surface is absent in the UAS DA experiment. Here, the UAS DA is influencing low-level moisture in a way that counteracts poor initialization of the soil moisture that is a main cause for the bias just above the surface.

At Moffat (CLAMPS location), there was a slightly weaker but deeper inversion than at the NSSL mobile sounding location at 1300 UTC (Fig. 13). The NoDA simulation predicts an inversion at this time, but it is too shallow. The UAS observations improve the predicted depth and strength of this inversion relative to the observations. The UAS DA simulation also removes the large dry bias and better captures the increasing relative humidity closer to the surface.

The UAS observations had a positive impact on the thermodynamic of the lower atmosphere at locations far from where the data were collected. Independent observations

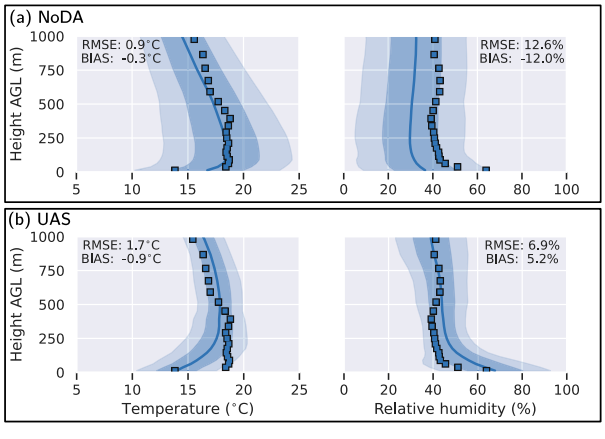

FIG. 12. As in Fig. 10, but for (left) temperature and (right) relative humidity.

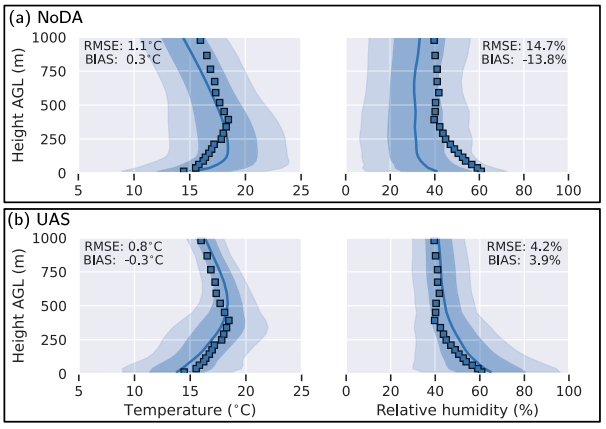

FIG. 13. As in Fig. 11, but for (left) temperature and (right) relative humidity.

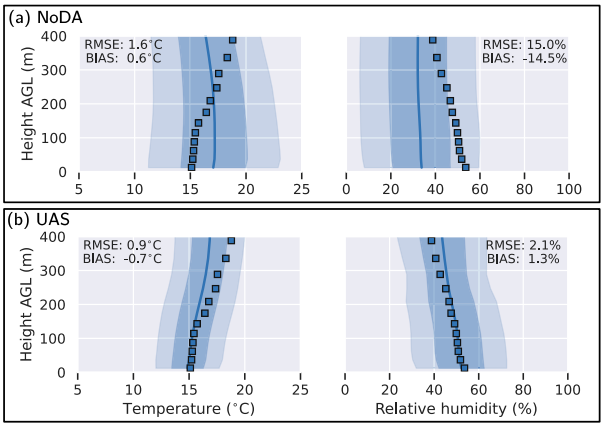

FIG. 14. Comparison of model profiles of (left) temperature and (right) relative humidity obtained with ensemble mean of priors and independent observations obtained with multirotor UAS flown at the OSU site at 1300 UTC. The RMSE and bias are given for this single comparison time.

obtained farther up the canyon by the OSU SOLO-I UAS (see Fig. 1) indicate that a weak inversion existed from the surface to 400 m AGL in the drainage source region (Fig. 14). The NoDA simulation does not capture this inversion and is too dry. UAS DA significantly improves the priors of both the temperature and humidity profiles by removing the low-level warm bias and better capturing the weak surface-based inversion. This notably reduces RMSE while maintaining a similar magnitude bias. Most impressive is the improved performance in relative humidity prediction. The −14.5% dry bias in NoDA is completely eliminated and the vertical gradient in relative humidity, which was missing from the NoDA predictions, is nearly replicated after UAS data are assimilated.

5. Assessment of UAS DA impact on free forecasts

To assess the impact of UAS DA on free forecasts of the evolving terrain-driven flows, the 1300 UTC ensemble mean analyses obtained from both the NoDA and UAS DA experiments are used to initialize free forecasts that were run for 4 h. Figure 15 shows the lowest model level v-wind component and wind barbs of the ensemble mean analysis valid at 1300 UTC. Winds are generally light in both simulations but much more variable in direction in the UAS DA analysis. Both analyses depict the northwesterly drainage component coming out of Saguache Canyon but the NoDA analysis extends the northwesterlies too far into the SLV compared to the mobile mesonet observations. These independent observations indicate the presence of easterly return flow that is also captured in the analysis obtained with UAS DA.

At 1430 UTC (1.5 h into the free forecast), southeasterly up-canyon flow is observed within the Saguache Canyon. Farther upstream, winds are easterly at the NSSL location sounding location and northeasterly at the MURC. To the south, drainage flow continues at del Norte while upvalley winds are occurring at Alamosa (Fig. 16). The flow field obtained with UAS DA compares much better to the observed flow field than that obtained with NoDA in the northern third of the SLV where UAS observations were collected. While the upvalley flow feature is clearly the main circulation at this time in both simulations, the wind direction associated with this flow differs between the two simulations with that in the UAS being more southerly (in better agreement with the observation at Alamosa and Moffat). Second, the wind direction at Saguache has reversed in the UAS assimilation but not in the NoDA simulation. In fact, the drainage flow is still prominent in the NoDA simulation at this time. Third, the area of northerlies and northeasterlies in the UAS DA run agree well with the observations at the MURC. There is a clear west-to-east gradient in winds in this area where the winds shift from northeasterly at the MURC location to southeasterly at Moffat. The NoDA simulation has no indication of these wind patterns with predominantly westerly winds in this area. Note that both simulations struggle with the drainage flow emanating from the del Norte Canyon, which is not surprising considering that UAS were not flown in this region.

Ultimately, over the course of the 4-h free forecasts the one initialized from the UAS DA analysis better predicted the evolution of temperature, relative humidity and winds at Saguache (Fig. 17). Importantly, the warm dry bias is greatly reduced throughout the 4-h free forecast and the sudden wind shift at 1400 UTC associated with the transition to up-canyon flow is well captured when UAS data are assimilated after just 1.5 h of cycling. This indicates that UAS DA has adjusted the initial model state enough to substantively improve key aspects of the simulation several hours into the future.

6. Discussion

One of the benefits of ensemble DA is that it provides the ability to quantify forecast uncertainty and to develop probabilistic products that assess the likelihood of an event. Here a probabilistic guidance product that depicts the likelihood of drainage winds across the SLV is presented. The probability is computed by counting the number of member priors (i.e., 15-min forecasts) with $u > 0$ and $v < 0\,\mathrm{m\,s^{-1}}$ and dividing by

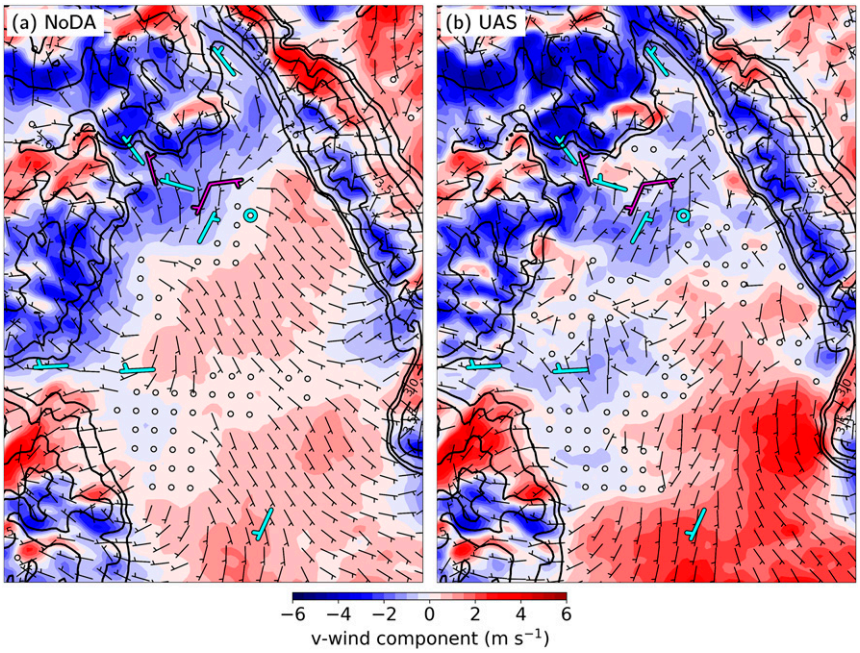

FIG. 15. Lowest-model-level (~13 m AGL) v-wind component (colored contours), wind barbs (black), and terrain heights (black contours lines) from the 1300 UTC analysis with (a) no assimilation and (b) UAS assimilation. The cyan wind barbs show wind observations from the lowest available observation height from the BST UAS (at Poncha Pass), the Windcube Doppler lidars at Saguache and Moffat, the NSSL sounding, and the surface observations from the MURC 18-m tower and the surface meteorological stations at Del Norte, Alamosa, and Center (see Fig. 1 for locations). The magenta wind barbs show additional wind observations obtained at three locations along a 15-min east–west–east transect by the UNL mobile mesonet. The half flags denote wind speeds of at least 1 m s^{-1}, and the open circles denote winds speeds of <1 m s^{-1}. The location of each barb is at its head.

the total number of members (40). It is evident that the assimilation of UAS observations increases the probability of drainage winds over NoDA and SFC DA both within Saguache Canyon and just to the south and west where the canyon empties into the SLV (Fig. 18). The drainage flow likelihood above the surface is even higher in the UAS DA case, but oddly lower in the SFC DA case. There are also notable differences in the distance drainage winds are likely to penetrate into the SLV. The NoDA simulation has probabilities exceeding 40% extending to the center of the northern SLV while both the SFC and UAS DA notably reduce the likelihood drainage winds extend much beyond the mouth of Saguache Canyon. In fact, the UAS DA simulation shows only a very low possibility of low-level drainage winds reaching the NSSL sounding location.

Observations discussed earlier indicate that there was a sharp cut off in the distance drainage winds extended into the SLV. Specifically, drainage winds were only observed at the westernmost segment of the mobile mesonet transects (Fig. 15) and only briefly reached the NSSL sounding launch site at 1300 UTC (Fig. 10) marked by the eastern star in Fig. 18. While probabilistic predictions require many realizations to verify, the impact of UAS DA seems to work in the correct direction both in terms of the enhanced likelihood of drainage winds in Saguache Canyon and with regard to the distance that the drainage flow extended into the SLV. Thus, UAS observations clearly improved the depiction of low-level drainage winds compared to results obtained with the NoDA and SFC DA experiments.

While UAS DA clearly improved the depiction of the drainage flow over both NoDA and SFC DA, biases in some of the UAS wind component observations may have limited the overall skill of the UAS DA analyses and forecasts. Correlated biases in the UAS wind component observations could have been caused by uncertainties or offsets in aircraft attitude or orientation or due to averaging used to upscale the high resolution UAS measurements to match the 1-km grid spacing or both; S. C. C. Bailey (2020, unpublished manuscript) found that the drainage winds observed with UAS on this day were strongest to the south of the Saguache AWOS station with reverse flow occurring just to the north of the AWOS station indicating the large horizontal variability in the drainage winds. Note also that the observational error variances were set to constant values in this study. Additional work is needed to assess the validity of this assumption by evaluating how observational uncertainties vary with platform type, profiling method and observational technique (especially for winds in which the components may be derived from aircraft motions or be computed from a multihole probe). Finally, there are also

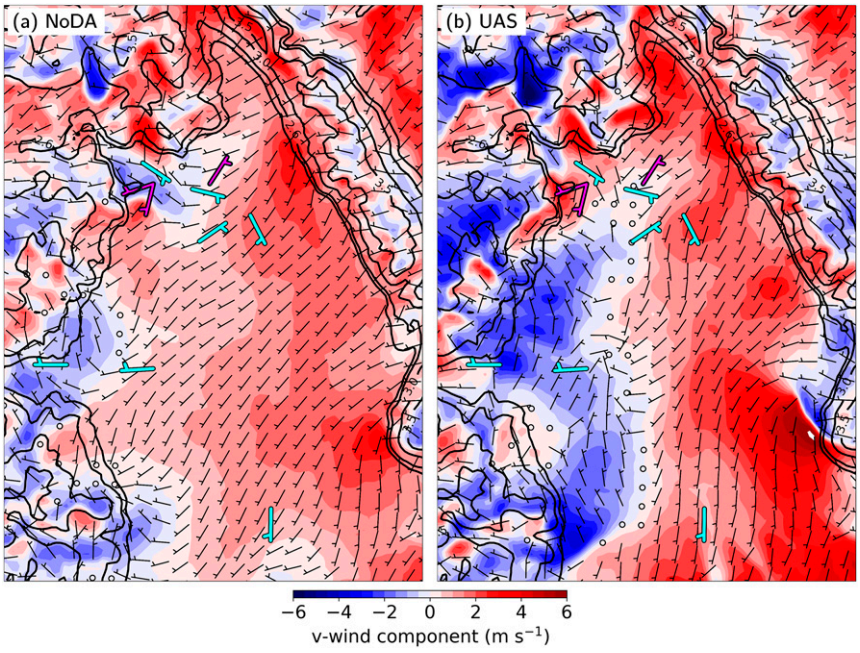

FIG. 16. As in Fig. 15, but 1.5 h into the free forecast (valid at 1430 UTC). The observation from the BST UAS is not available at this time. The magenta wind barbs show wind observations obtained at three locations along a 15-min west–east–west transect by the UNL mobile mesonet.

likely observational error covariances that should be explored (e.g., relative humidity error may have a temperature dependence) and incorporated into the error estimate used to perform EAKF.

The ability to accurately represent local properties of drainage flows (e.g., within a narrowing canyon) and their coupling with large-scale flows within a DA framework is challenging due to the need to correctly represent variability across a range of scales. The UAS DA simulation better captured the magnitude of the early morning inversion, but the cooling is spread over a layer that is three times deeper than observed (Fig. 12). This bias may have been caused by the treatment of vertical diffusion under stable stratification by the PBL scheme. Supporting this hypothesis is evidence from a real-time LES simulation of this same drainage flow case that reveals that a more explicit treatment of the boundary layer could better capture this shallow inversion (Pinto et al. 2021). However, for assimilation of UAS DA into mesoscale models additional studies using less diffusive PBL schemes (e.g., Olson et al. 2019a) are warranted.

The key point here, is that as UAS collect observations of increasing spatiotemporal resolution, and these data are assimilated at ever more fine grid spacings, the response of parameterizations must be evaluated and may reveal biases that were previously hidden. As such, as modeling moves toward finer scales, UAS observations and UAS DA can be used to verify and improve physical parameterizations such as PBL schemes, surface-layer treatments and impacts of land surface heterogeneities. As we have shown in this study, based on evaluation of analyses that result from UAS DA, it appears the PBL scheme employed was likely too diffusive. However, more systematic evaluations over a longer period of time are needed to fully quantify biases and their dependencies on physical parameterizations following the methodology of Wong et al. (2020). An important consideration moving

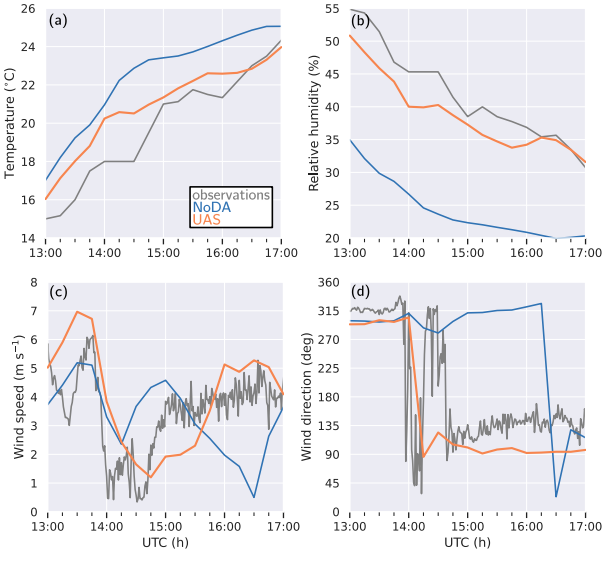

FIG. 17. Time series from 4-h-long free forecasts of 2-m (a) air temperature and (b) relative humidity and 40-m (c) wind speed and (d) wind direction at Saguache initialized with the 1300 UTC analysis ensemble mean with no assimilation (blue) and UAS assimilation (orange). Observations (gray) are from the Saguache AWOS in (a) and (b) and the 1-min 40-m AGL lidar return in (c) and (d). The model winds are taken from the second vertical level, which is nominally at 40 m AGL.

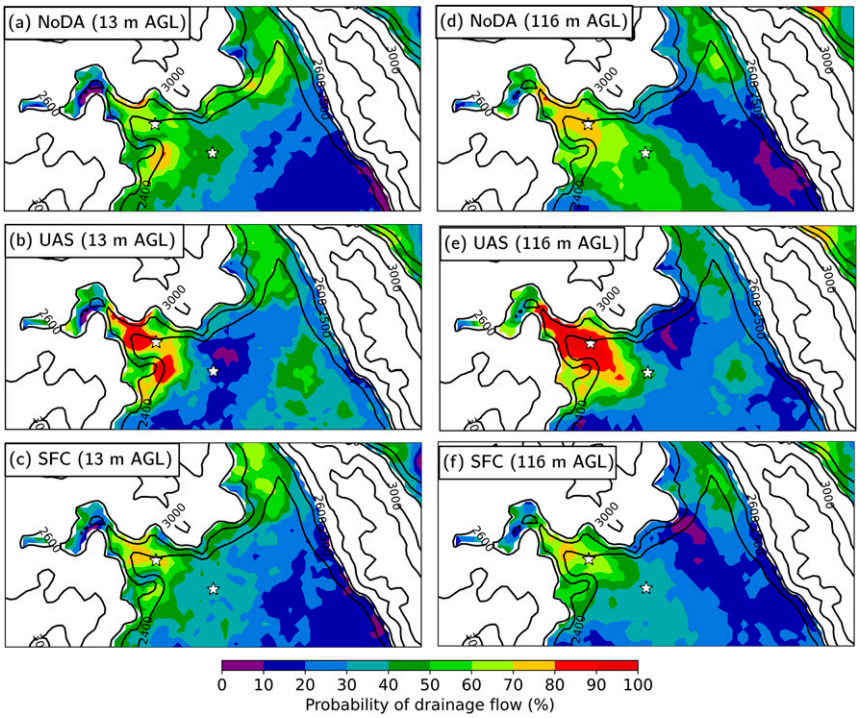

FIG. 18. Probability of drainage flow at the lowest model level at 1300 UTC for (a) NoDA, (b) UAS assimilation, and (c) SFC assimilation. (d)–(f) As in (a)–(c), but at 116 m AGL. The white stars show the locations of Saguache and the NSSL soundings. The probabilities are only shown in the SLV (terrain height < 2600 m).

forward with fine-scale UAS DA is that most parameterizations are not necessarily designed to be run at increasingly higher resolutions (scale aware) and may need to be adapted (e.g., Frassoni et al. 2018; Jeworrek et al. 2019) to improve the influence of fine-scale DA, particularly within the boundary layer where observations from small UAS will be coming online. The development of scale-aware parameterizations to represent boundary layer processes is an area of active research (e.g., Shin and Hong 2015; Choi and Han 2020; Kosović et al. 2020) that will need to be interwoven with fine-scale UAS DA in the PBL.

7. Summary and conclusions

The impact of assimilating UAS observations on the accuracy of analyses and the skill of short-term predictions of terrain-influenced mesoscale flows in a high alpine desert has been assessed. Observations from a fleet of small UAS were assimilated using an EAKF. To the authors' knowledge this study represents the first attempt to use EAKF to assimilate observations obtained with several coordinated small UAS. Experiments were conducted to explore the impact of UAS observations on predictions of low-level (below 1 km AGL) temperature, humidity and wind profiles during the transition from nocturnal to daytime boundary layer and associated evolving flow patterns.

The utility of DA was quantified by evaluating the 15-min forecasts (priors). UAS DA generally reduced both RMSE and bias in the 15-min forecasts of temperature, winds and humidity by over 40% versus the NoDA benchmark. In addition, the timing, strength and horizontal extent of the drainage winds are much better depicted in the UAS DA simulation than that obtained with both the NoDA and SFC DA experiments. UAS DA was particularly important for correctly predicting the timing of the transition from drainage to upvalley flow in longer free forecast while reducing biases in surface air temperature, relative humidity and winds for lead times of up to 4 h. In future work, OSE studies will be performed to further evaluate the benefit of UAS observations relative to surface observations for cases observed during LAPSE-RATE.

The favorable impact of UAS DA on the accuracy of analyses and predictions have been demonstrated at the mesogamma-scale. Given the scale over which UAS observations were collected, it is unlikely that their net positive influence will have improved analyses much farther beyond their region of influence as defined by localization, although more sensitivity studies with varying localization values and varying other relevant DA parameters would be useful future work. As discussed, increased accuracy in the free forecast persisted for about 4 h, which is consistent with mesogamma-scale improvements. However, observing system simulation experiment (OSSE) studies have indicated that more widespread distribution of UAS sampling (as one might achieve either through dedicated weather UAS or leveraged from widespread commercial operations with symbiotic reporting of weather data) could significantly improve other predictions at much

larger scales (Chilson et al. 2019). While OSSEs can be performed (using simulated weather and observing system data) across a range of environments to assess the value of new observing system and to evaluate and optimize sampling strategies, OSEs are also needed to demonstrate that these benefits are indeed achievable in practice with real weather and real observations. Additional research with both OSSEs and OSEs are needed to fully assess the potential value of UAS DA under a range of environmental conditions. Key to these studies will be a discussion on how these improvements to the accuracy of predictions afforded by UAS DA can be translated to improve decision-making and thus economic value across a range of industries.

As the need for accurate high-resolution predictions of weather continues to grow, more accurate mesoscale analyses and predictions will be needed to initialize and drive the lateral boundaries of the next generation of meso- to microscale modeling systems (Haupt et al. 2019). The need for more detailed weather information spans a number of economic sectors. Agricultural practices and wind energy resource management rely on accurate and detailed predictions of low-level winds for irrigation and crop maintenance as well as wind energy prediction. Likewise, commercial UAS delivery and infrastructure inspection services require a high-resolution depiction of low-level winds for flight planning (Campbell et al. 2017; Roseman and Argrow 2020). Fine-scale variability in winds resulting from local circulations and boundary layer structures is inherently less predictable than variability resulting from larger-scale forcing. Thus, as the need for fine-scale analyses and predictions of low-level winds and weather continues to expand, so will the need for forecast uncertainty information. As demonstrated in this study, the EnKF DA approach provides an excellent framework for both improving mesoscale predictions via UAS DA and providing an estimate of analysis and forecast uncertainty.

Assimilation of observations from commercial UAS (e.g., Fleischer 2019) coupled with those obtained with new UAS weather observing networks, such as the 3D mesonet proposed by Chilson et al. (2019), could result in a notable jump in the skill and reduction of uncertainty in mesoscale analyses and resulting fine-scale predictions. As such, commercial UAS could help to improve the weather predictions they and other economic sectors require, analogous to the impact of observations collected with commercial aircraft today (James and Benjamin 2017). This more accurate depiction of mesoscale flows is needed to drive the next generation of resident-GPU LES models (e.g., Sauer and Muñoz-Esparza 2020) that will ultimately provide probabilistic microscale predictions in real time.

Acknowledgments. We thank Pedro Jiménez for help in setting up the initial configuration of the Weather Research and Forecast Model used in this study. The surface meteorological data were obtained from the Iowa Environmental Mesonet at Iowa State University and Colorado State University CoAgMET mesonet data archive. The authors are also appreciative of the National Center for Atmospheric Research Computational and Information Systems Laboratory (CISL)'s support of the Cheyenne and Casper supercomputers used to produce the simulations. The National Center for Atmospheric Research is sponsored by the National Science Foundation. This work was specifically supported in part by NSF Award AGS-1755088. Julie Lundquist's contribution to this paper was funded, in part, by the National Renewable Energy Laboratory, operated by Alliance for Sustainable Energy, LLC, for the U.S. Department of Energy (DOE) under Contract DE-AC36-08GO28308 via the Office of Energy Efficiency and Renewable Energy Wind Energy Technologies. The views expressed in the article do not necessarily represent the views of the DOE or the U.S. government. The publisher, by accepting the article for publication, acknowledges that the U.S. government retains a nonexclusive, paid-up, irrevocable, worldwide license to publish or reproduce the published form of this work, or allow others to do so, for U.S. government purposes. Gijs de Boer was supported by the NOAA/Physical Sciences Laboratory. Support for the LAPSE-RATE campaign was provided by the International Society for Atmospheric Research using Remotely Piloted Aircraft (ISARRA), with the U.S. National Science Foundation (NSF AGS 1807199) and the U.S. DOE (DE-SC0018985) supporting the participation of early career scientists. This work was also supported, in part, by the NASA University Leadership Initiative (ULI) under Award 80NSSC20M0162.

Data availability statement. Data assimilation simulations have been archived on CISL's 5-year campaign storage system and are available upon request. UAS observations are available online (https://zenodo.org/communities/lapse-rate/).

REFERENCES

Ágústsson, H., H. Ólafsson, M. O. Jonassen, and O. Rögnvaldsson, 2014: The impact of assimilating data from a remotely piloted aircraft on simulations of weak-wind orographic flow. *Tellus*, **66A**, 25421, https://doi.org/10.3402/tellusa.v66.25421.

Anderson, J. L., 2001: An ensemble adjustment Kalman filter for data assimilation. *Mon. Wea. Rev.*, **129**, 2884–2903, https://doi.org/10.1175/1520-0493(2001)129<2884:AEAKFF>2.0.CO;2.

——, 2012: Localization and sampling error correction in ensemble Kalman filter data assimilation. *Mon. Wea. Rev.*, **140**, 2359–2371, https://doi.org/10.1175/MWR-D-11-00013.1.

——, T. Hoar, K. Raeder, H. Liu, N. Collins, R. Torn, and A. Avellano, 2009: The Data Assimilation Research Testbed: A community facility. *Bull. Amer. Meteor. Soc.*, **90**, 1283–1296, https://doi.org/10.1175/2009BAMS2618.1.

Bailey, S. C., S. W. Smith, and M. P. Sama, 2020a: University of Kentucky files from LAPSE-RATE. Zenodo, accessed 5 August 2020, https://doi.org/10.5281/zenodo.3923056.

——, and Coauthors, 2020b: University of Kentucky measurements of wind, temperature, pressure and humidity in support of LAPSE-RATE using multi-site fixed-wing and rotorcraft unmanned aerial systems. *Earth Syst. Sci. Data*, **12**, 1759–1773, https://doi.org/10.5194/essd-12-1759-2020.

Banta, R. M., and Coauthors, 1997: Nocturnal cleansing flows in a tributary valley. *Atmos. Environ.*, **31**, 2147–2162, https://doi.org/10.1016/S1352-2310(96)00359-7.

Barbieri, L., and Coauthors, 2019: Intercomparison of small unmanned aircraft system (sUAS) measurements for atmospheric science during the LAPSE-RATE campaign. *Sensors (Basel)*, **19**, 2179, https://doi.org/10.3390/s19092179.

Bell, T. M., and P. Klein, 2020: OU/NSSL CLAMPS Doppler lidar data from LAPSE-RATE. Zenodo, accessed 5 August 2020, https://doi.org/10.5281/zenodo.3780623.

——, ——, and D. Turner, 2020a: OU/NSSL CLAMPS microwave radiometer and surface meteorological data from LAPSE-RATE. Zenodo, accessed 5 August 2020, https://doi.org/10.5281/zenodo.3780593.

——, B. R. Greene, P. M. Klein, M. Carney, and P. B. Chilson, 2020b: Confronting the boundary layer data gap: Evaluating new and existing methodologies of probing the lower atmosphere. *Atmos. Meas. Tech.*, **13**, 3855–3872, https://doi.org/10.5194/amt-13-3855-2020.

——, P. M. Klein, J. K. Lundquist, and S. Waugh, 2021: Remote sensing and radiosonde datasets collected in the San Luis Valley during the LAPSE-RATE campaign. *Earth Syst. Sci. Data*, **13**, 1041–1051, https://doi.org/10.5194/essd-13-1041-2021.

Benjamin, S. G., B. D. Jamison, W. R. Moninger, S. R. Sahm, B. E. Schwartz, and T. W. Schlatter, 2010: Relative short-range forecast impact from aircraft, profiler, radiosonde, VAD, GPS-PW, METAR, and mesonet observations via the RUC hourly assimilation cycle. *Mon. Wea. Rev.*, **138**, 1319–1343, https://doi.org/10.1175/2009MWR3097.1.

——, and Coauthors, 2016: A North American hourly assimilation and model forecast cycle: The Rapid Refresh. *Mon. Wea. Rev.*, **144**, 1669–1694, https://doi.org/10.1175/MWR-D-15-0242.1.

Bergen, J. D., 1969: Cold air drainage on a forested mountain slope. *J. Appl. Meteor.*, **8**, 884–895, https://doi.org/10.1175/1520-0450(1969)008<0884:CADOAF>2.0.CO;2.

Brousseau, P., L. Berre, F. Bouttier, and G. Desroziers, 2012: Flow-dependent background-error covariances for a convective-scale data assimilation system. *Quart. J. Roy. Meteor. Soc.*, **138**, 310–322, https://doi.org/10.1002/qj.920.

Campbell, S. E., D. A. Clark, and J. E. Evans, 2017: Preliminary weather information gap analysis for UAS operations. MIT Lincoln Laboratory Tech. Rep. ATC-437, 126 pp., https://www.ll.mit.edu/sites/default/files/publication/doc/2018-05/Campbell_2017_ATC- 437.pdf.

Cardinali, C., L. Isaksen, and E. Andersson, 2003: Use and impact of automated aircraft data in a global 4DVAR data assimilation system. *Mon. Wea. Rev.*, **131**, 1865–1877, https://doi.org/10.1175//2569.1.

Cassano, J. J., 2014: Observations of atmospheric boundary layer temperature profiles with a small unmanned aerial vehicle. *Antarct. Sci.*, **26**, 205–213, https://doi.org/10.1017/S0954102013000539.

Chen, F., and Coauthors, 1996: Modeling of land surface evaporation by four schemes and comparison with FIFE observations. *J. Geophys. Res.*, **101**, 7251–7268, https://doi.org/10.1029/95JD02165.

Chilson, P. B., and Coauthors, 2019: Moving towards a network of autonomous UAS atmospheric profiling stations for observations in the earth's lower atmosphere: The 3D mesonet concept. *Sensors*, **19**, 2720, https://doi.org/10.3390/s19122720.

Choi, H.-J., and J.-Y. Han, 2020: Effect of scale-aware nonlocal planetary boundary layer scheme on lake-effect precipitation at gray-zone resolutions. *Mon. Wea. Rev.*, **148**, 2761–2776, https://doi.org/10.1175/MWR-D-19-0282.1.

Cione, J. J., E. A. Kalina, E. W. Uhlhorn, A. M. Farber, and B. Damiano, 2016: Coyote unmanned aircraft system observations in Hurricane Edouard (2014). *Earth Space Sci.*, **3**, 370–380, https://doi.org/10.1002/2016EA000187.

——, and Coauthors, 2020: Eye of the storm: Observing hurricanes with a small unmanned aircraft system. *Bull. Amer. Meteor. Soc.*, **101**, E186–E205, https://doi.org/10.1175/BAMS-D-19-0169.1.

Coen, J. L., M. Cameron, J. Michalakes, E. G. Patton, P. J. Riggan, and K. M. Yedinak, 2013: WRF-Fire: Coupled weather–wildland fire modeling with the Weather Research and Forecasting Model. *J. Appl. Meteor. Climatol.*, **52**, 16–38, https://doi.org/10.1175/JAMC-D-12-023.1.

Curry, J. A., J. Maslanik, G. Holland, and J. Pinto, 2004: Applications of aerosondes in the Arctic. *Bull. Amer. Meteor. Soc.*, **85**, 1855–1862, https://doi.org/10.1175/BAMS-85-12-1855.

de Boer, G., and Coauthors, 2018: A bird's-eye view: Development of an operational ARM unmanned aerial capability for atmospheric research in Arctic Alaska. *Bull. Amer. Meteor. Soc.*, **99**, 1197–1212, https://doi.org/10.1175/BAMS-D-17-0156.1.

——, S. Borenstein, C. Dixon, and B. Argrow, 2020a: University of Colorado MURC observations from LAPSE-RATE. Zenodo, accessed 5 August 2020, https://doi.org/10.5281/zenodo.3875493.

——, D. Lawrence, and A. Doddi, 2020b: DataHawk2 files from LAPSE-RATE. Zenodo, accessed 5 August 2020, https://doi.org/10.5281/zenodo.3891620.

——, and Coauthors, 2020c: Data generated during the 2018 LAPSE-RATE campaign: An introduction and overview. *Earth Syst. Sci. Data*, **12**, 3357–3366, https://doi.org/10.5194/essd-12-3557-2020.

——, and Coauthors, 2020d: Development of community, capabilities, and understanding through unmanned aircraft-based atmospheric research: The LAPSE-RATE campaign. *Bull. Amer. Meteor. Soc.*, **101**, E684–E699, https://doi.org/10.1175/BAMS-D-19-0050.1.

——, and Coauthors, 2021a: University of Colorado and Black Swift Technologies RPAS-based measurements of the lower atmosphere during LAPSE-RATE. *Earth Syst. Sci. Data*, https://doi.org/10.5194/ESSD-2020-333, in press.

——, S. Waugh, A. Erwin, S. Borenstein, C. Dixon, W. Shanti, A. Houston, and B. Argrow, 2021b: Measurements from mobile surface vehicles during the Lower Atmospheric Profiling Studies at Elevation—a Remotely-Piloted Aircraft Team Experiment (LAPSE-RATE). *Earth Syst. Sci. Data*, **13**, 155–169, https://doi.org/essd-13-155-201.

Defant, F., 1951: Local winds. *Compendium of Meteorology*, T. F. Malone, Ed., Amer. Meteor. Soc., 655–672.

Dimitrova, R., Z. Silver, H. J. S. Fernando, L. Leo, S. D. Sabatino, C. Hocut, and T. Zsedrovits, 2014: Inter-comparison between different PBL options in WRF model: Modification of two PBL schemes for stable conditions. *18th Joint Conference on the Applications of Air Pollution Meteorology with the A&WMA*, Atlanta, GA, Amer. Meteor. Soc., 16.3, https://ams.confex.com/ams/94Annual/webprogram/Paper230298.html.

Dirren, S., R. D. Torn, and G. J. Hakim, 2007: A data assimilation case study using a limited-area ensemble Kalman filter. *Mon. Wea. Rev.*, **135**, 1455–1473, https://doi.org/10.1175/MWR3358.1.

Doran, C., J. Fast, and H. John, 2002: The VTMX 2000 campaign. *Bull. Amer. Meteor. Soc.*, **83**, 537–554, https://doi.org/10.1175/1520-0477(2002)083<0537:TVC>2.3.CO;2.

Duan, B., W. Zhang, and H. Dai, 2018: ASCAT wind superobbing based on feature box. *Adv. Meteor.*, **2018**, 1–10, https://doi.org/10.1155/2018/3438501.

Dutton, J. A., 2002: Opportunities and priorities in a new era for weather and climate services. *Bull. Amer. Meteor. Soc.*, **83**, 1303–1312, https://doi.org/10.1175/1520-0477-83.9.1303.

Easton, Z. M., and Coauthors, 2017: Short-term forecasting tools for agricultural nutrient management. *J. Environ. Qual.*, **46**, 1257–1269, https://doi.org/10.2134/jeq2016.09.0377.

Elston, J., and M. Stachura, 2020: Black Swift Technologies S1 unmanned aircraft system observations from LAPSE-RATE. Zenodo, accessed 5 August 2020, https://doi.org/10.5281/zenodo.3861831.

——, B. Argrow, M. Stachura, D. Weibel, D. Lawrence, and D. Pope, 2015: Overview of small fixed-wing unmanned aircraft for meteorological sampling. *J. Atmos. Oceanic Technol.*, **32**, 97–115, https://doi.org/10.1175/JTECH-D-13-00236.1.

Elston, J. S., J. Roadman, M. Stachura, B. Argrow, A. Houston, and E. Frew, 2011: The tempest unmanned aircraft system for in situ observations of tornadic supercells: Design and VORTEX2 flight results. *J. Field Robot.*, **28**, 461–483, https://doi.org/10.1002/rob.20394.

FAA, 2020: Unmanned aircraft systems. *FAA Aerospace Forecast: Fiscal Years 2020–2040*. Federal Aviation Administration, 41–63, https://www.faa.gov/data_research/aviation/aerospace_forecasts/media/Unmanned_Aircraft_Systems.pdf.

Flagg, D. D., and Coauthors, 2018: On the impact of unmanned aerial system observations on numerical weather prediction in the coastal zone. *Mon. Wea. Rev.*, **146**, 599–622, https://doi.org/10.1175/MWR-D-17-0028.1.

Fleischer, L., 2019: Weather impacts on medical supply deliveries. Preprints, *Unmanned Aerial System (UAS) Weather Forum*, Chicago, IL, National Center for Atmospheric Research, 33 pp., https://ral.ucar.edu/sites/default/files/public/events/2019/unmanned-aerial-system-uas-weather-forum/docs/2-presentation-fleischer.pdf.

Frassoni, A., and Coauthors, 2018: Building the next generation of climate modelers: Scale-aware physics parameterization and the "gray zone" challenge. *Bull. Amer. Meteor. Soc.*, **99**, ES185–ES189, https://doi.org/10.1175/BAMS-D-18-0145.1.

Frew, E. W., B. Argrow, S. Borenstein, S. Swenson, C. A. Hirst, H. Havenga, and A. Houston, 2020: Field observation of tornadic supercells by multiple autonomous fixed-wing unmanned aircraft. *J. Field Rob.*, **37**, 1077–1093, https://doi.org/10.1002/rob.21947.

Garrett-Glaser, B., 2020: Are low-altitude weather services ready for drones and air taxis? *Aviation Today*, 26 April 2020, https://www.aviationtoday.com/2020/04/26/low-altitude-weather-services-ready-drones-air-taxis/.

Glasheen, K., J. Pinto, M. Steiner, and E. Frew, 2020: Assessment of finescale local wind forecasts using small unmanned aircraft systems. *J. Aerosp. Inform. Syst.*, **17**, 182–192, https://doi.org/10.2514/1.I010747.

Greene, B. R., A. R. Segales, T. M. Bell, E. A. Pillar-Little, and P. B. Chilson, 2019: Environmental and sensor integration influences on temperature measurements by rotary-wing unmanned aircraft systems. *Sensors*, **19**, 1470, https://doi.org/10.3390/s19061470.

——, and Coauthors, 2020: University of Oklahoma CopterSonde files from LAPSE-RATE. Zenodo, accessed 5 August 2020, https://doi.org/10.5281/zenodo.3737087.

Ha, S.-Y., and C. Snyder, 2014: Influence of surface observations in mesoscale data assimilation using an ensemble Kalman filter. *Mon. Wea. Rev.*, **142**, 1489–1508, https://doi.org/10.1175/MWR-D-13-00108.1.

Hacker, J., C. Draper, and L. Madaus, 2018: Challenges and opportunities for data assimilation in mountainous environments. *Atmosphere*, **9**, 127, https://doi.org/10.3390/atmos9040127.

Haupt, S. E., and Coauthors, 2019: On bridging a modeling scale gap: Mesoscale to microscale coupling for wind energy. *Bull. Amer. Meteor. Soc.*, **100**, 2533–2550, https://doi.org/10.1175/BAMS-D-18-0033.1.

Hildmann, H., E. Kovacs, F. Saffre, and A. F. Isakovic, 2019: Nature-inspired drone swarming for real-time aerial data-collection under dynamic operational constraints. *Drones*, **3**, 71, https://doi.org/10.3390/drones3030071.

Hong, S.-Y., and J.-O. J. Lim, 2006: The WRF single-moment 6-class microphysics scheme (wsm6). *J. Korean Meteor. Soc.*, **42**, 129–151.

Houston, A. L., and A. Erwin, 2020: University of Nebraska-Lincoln mobile mesonet files from LAPSE-RATE. Zenodo, accessed 5 August 2020, https://doi.org/10.5281/zenodo.3838724.

——, B. Argrow, J. Elston, J. Lahowetz, E. W. Frew, and P. C. Kennedy, 2012: The Collaborative Colorado–Nebraska Unmanned Aircraft System Experiment. *Bull. Amer. Meteor. Soc.*, **93**, 39–54, https://doi.org/10.1175/2011BAMS3073.1.

Iacono, M. J., J. S. Delamere, E. J. Mlawer, M. W. Shephard, S. A. Clough, and W. D. Collins, 2008: Radiative forcing by long-lived greenhouse gases: Calculations with the AER radiative transfer models. *J. Geophys. Res.*, **113**, D13103, https://doi.org/10.1029/2008JD009944.

Ives, R. L., 1939: "River fogs" of Middle Park, Colorado. *Bull. Amer. Meteor. Soc.*, **20**, 415–417, https://doi.org/10.1175/1520-0477-20.9.415.

Jacob, J., V. Natalie, A. Avery, C. Crick, B. Hemingway, and A. Frazier, 2020: Oklahoma State University files from LAPSE-RATE: Part 1. Zenodo, accessed 5 August 2020, https://doi.org/10.5281/zenodo.3700749.

James, E. P., and S. G. Benjamin, 2017: Observation system experiments with the hourly updating Rapid Refresh model using GSI hybrid ensemble–variational data assimilation. *Mon. Wea. Rev.*, **145**, 2897–2918, https://doi.org/10.1175/MWR-D-16-0398.1.

——, ——, and B. D. Jamison, 2020: Commercial-aircraft-based observations for NWP: Global coverage, data impacts, and COVID-19. *J. Appl. Meteor. Climatol.*, **59**, 1809–1825, https://doi.org/10.1175/JAMC-D-20-0010.1.

Jeworrek, J., G. West, and R. Stull, 2019: Evaluation of cumulus and microphysics parameterizations in WRF across the convective gray zone. *Wea. Forecasting*, **34**, 1097–1115, https://doi.org/10.1175/WAF-D-18-0178.1.

Jiménez, P. A., D. Muñoz-Esparza, and B. Kosović, 2018: A high resolution coupled fire–atmosphere forecasting system to minimize the impacts of wildland fires: Applications to the Chimney Tops II wildland event. *Atmosphere*, **9**, 197, https://doi.org/10.3390/atmos9050197.

Jonassen, M. O., H. Olafsson, H. Agústsson, O. Rögnvaldsson, and J. Reuder, 2012: Improving high-resolution numerical weather simulations by assimilating data from an unmanned aerial system. *Mon. Wea. Rev.*, **140**, 3734–3756, https://doi.org/10.1175/MWR-D-11-00344.1.

Kosović, B., P. J. Munoz, T. W. Juliano, A. Martilli, M. Eghdami, A. P. Barros, and S. E. Haupt, 2020: Three-dimensional planetary boundary layer parameterization for high-resolution mesoscale simulations. *J. Phys. Conf. Series*, **1452**, 012080, https://doi.org/10.1088/1742-6596/1452/1/012080.

Lei, L., J. S. Whitaker, J. L. Anderson, and Z. Tan, 2020: Adaptive localization for satellite radiance observations in an ensemble Kalman filter. *J. Adv. Model. Earth Syst.*, **12**, e2019MS001693, https://doi.org/10.1029/2019MS001693.

Leuenberger, D., A. Haefele, N. Omanovic, M. Fengler, G. Martucci, B. Calpini, O. Fuhrer, and A. Rossa, 2020:

Improving high-impact numerical weather prediction with lidar and drone observations. *Bull. Amer. Meteor. Soc.*, **101**, E1036–E1051, https://doi.org/10.1175/BAMS-D-19-0119.1.

Lundquist, J. K., P. Murphy, and C. Plunkett, 2020: LAPSE-RATE ground-based Doppler lidar datasets from University of Colorado Boulder. Zenodo, accessed 5 August 2020, https://doi.org/10.5281/zenodo.3804164.

Mlawer, E. J., S. J. Taubman, P. D. Brown, M. J. Iacono, and S. A. Clough, 1997: Radiative transfer for inhomogeneous atmospheres: RRTM, a validated correlated-*k* model for the longwave. *J. Geophys. Res.*, **102**, 16 663–16 682, https://doi.org/10.1029/97JD00237.

Muñoz-Esparza, D., R. Sharman, J. Sauer, and B. Kosović, 2018: Toward low-level turbulence forecasting at eddy-resolving scales. *Geophys. Res. Lett.*, **45**, 8655–8664, https://doi.org/10.1029/2018GL078642.

Nakanishi, M., and H. Niino, 2009: Development of an improved turbulence closure model for the atmospheric boundary layer. *J. Meteor. Soc. Japan*, **87**, 895–912, https://doi.org/10.2151/jmsj.87.895.

Necker, T., M. Weissmann, and Y. Ruckstuhl, J. Anderson, and T. Miyoshi, 2020: Sampling error correction evaluated using a convective-scale 1000-member ensemble. *Mon. Wea. Rev.*, **148**, 1229–1249, https://doi.org/10.1175/MWR-D-19-0154.1.

Neff, W. D., and C. W. King, 1989: The accumulation and pooling of drainage flows in a large basin. *J. Appl. Meteor.*, **28**, 518–529, https://doi.org/10.1175/1520-0450(1989)028<0518:TAAPOD>2.0.CO;2.

Olson, J. B., J. S. Kenyon, W. A. Angevine, J. M. Brown, M. Pagowski, and K. Suselj, 2019a: A description of the MYNN-EDMF scheme and the coupling to other components in WRF–ARW. NOAA Tech. Memo. OAR GSD-61, 42 pp., https://doi.org/10.25923/n9wm-be49.

——, and Coauthors, 2019b: Improving wind energy forecasting through numerical weather prediction model development. *Bull. Amer. Meteor. Soc.*, **100**, 2201–2220, https://doi.org/10.1175/BAMS-D-18-0040.1.

Orville, H. D., 1964: On mountain upslope winds. *J. Atmos. Sci.*, **21**, 622–633, https://doi.org/10.1175/1520-0469(1964)021<0622:OMUW>2.0.CO;2.

Parrish, D. F., and J. C. Derber, 1992: The National Meteorological Center's spectral statistical-interpolation analysis system. *Mon. Wea. Rev.*, **120**, 1747–1763, https://doi.org/10.1175/1520-0493(1992)120<1747:TNMCSS>2.0.CO;2.

Petersen, R. A., 2016: On the impact and benefits of AMDAR observations in operational forecasting—Part I: A review of the impact of automated aircraft wind and temperature reports. *Bull. Amer. Meteor. Soc.*, **97**, 585–602, https://doi.org/10.1175/BAMS-D-14-00055.1.

——, L. Cronce, R. Mamrosh, R. Baker, and P. Pauley, 2016: On the impact and future benefits of AMDAR observations in operational forecasting: Part II: Water vapor observations. *Bull. Amer. Meteor. Soc.*, **97**, 2117–2133, https://doi.org/10.1175/BAMS-D-14-00211.1.

Pillar-Little, E. A., and Coauthors, 2021: Observations of the thermodynamic and kinematic state of the atmospheric boundary layer over the San Luis Valley, CO, using the CopterSonde 2 remotely piloted aircraft system in support of the LAPSE-RATE field campaign. *Earth Syst. Sci. Data*, **13**, 269–280, https://doi.org/10.5194/essd-13-269-2021.

Pinto, J. O., D. B. Parsons, W. O. J. Brown, S. Cohn, N. Chamberlain, and B. Morley, 2006: Coevolution of down-valley flow and the nocturnal boundary layer in complex terrain. *J. Appl. Meteor. Climatol.*, **45**, 1429–1449, https://doi.org/10.1175/JAM2412.1.

——, A. A. Jensen, P. A. Jiménez, T. Hertneky, D. Muñoz-Esparza, A. Dumont, and M. Steiner, 2021: Real-time WRF large-eddy simulations to support uncrewed aircraft system (UAS) flight planning and operations during 2018 LAPSE-RATE. *Earth Syst. Sci. Data*, **13**, 697–711, https://doi.org/10.5194/eesd-13-697-2021.

Powers, J. G., and Coauthors, 2017: The Weather Research and Forecasting model: Overview, system efforts, and future directions. *Bull. Amer. Meteor. Soc.*, **98**, 1717–1737, https://doi.org/10.1175/BAMS-D-15-00308.1.

Rampanelli, G., D. Zardi, and R. Rotunno, 2004: Mechanisms of up-valley winds. *J. Atmos. Sci.*, **61**, 3097–3111, https://doi.org/10.1175/JAS-3354.1.

Reymann, C., A. Renzaglia, F. Lamraoui, M. Bronz, and S. Lacroix, 2018: Adaptive sampling of cumulus clouds with UAVs. *Auton. Robots*, **42**, 491–512, https://doi.org/10.1007/s10514-017-9625-1.

Robinson, M., M. Fronzak, M. Steiner, M. Huberdeau, and T. Becher, 2020: What if every aeronautical vehicle operating in our airspace were to report weather conditions? *20th Conf. on Aviation, Range and Aerospace Meteorology*, Boston, MA, Amer. Metero. Soc., 28 pp, https://ams.confex.com/ams/2020Annual/webprogram/Manuscript/Paper369277/U-ABO_Final.pdf.

Romine, G. S., C. S. Schwartz, C. Snyder, J. L. Anderson, and M. L. Weisman, 2013: Model bias in a continuously cycled assimilation system and its influence on convection-permitting forecasts. *Mon. Wea. Rev.*, **141**, 1263–1284, https://doi.org/10.1175/MWR-D-12-00112.1.

Roseman, C. A., and B. M. Argrow, 2020: Weather hazard risk quantification for sUAS safety risk management. *J. Atmos. Oceanic Technol.*, **37**, 1251–1268, https://doi.org/10.1175/JTECH-D-20-0009.1.

Sauer, J. A., and D. Muñoz-Esparza, 2020: The FastEddy resident-GPU accelerated large-eddy simulation framework: Model formulation, dynamical-core validation and performance benchmarks. *J. Adv. Model. Earth Syst.*, **12**, e2020MS002100, https://doi.org/10.1029/2020MS002100.

Schwartz, C. S., G. S. Romine, R. A. Sobash, K. R. Fossell, and M. L. Weisman, 2019: NCAR's real-time convection-allowing ensemble project. *Bull. Amer. Meteor. Soc.*, **100**, 321–343, https://doi.org/10.1175/BAMS-D-17-0297.1.

Shin, H. H., and S.-Y. Hong, 2011: Intercomparison of planetary boundary-layer parameterizations in the WRF model for a single day from CASES-99. *Bound.-Layer Meteor.*, **139**, 261–281, https://doi.org/10.1007/s10546-010-9583-z.

——, and ——, 2015: Representation of the subgrid-scale turbulent transport in convective boundary layers at gray-zone resolutions. *Mon. Wea. Rev.*, **143**, 250–271, https://doi.org/10.1175/MWR-D-14-00116.1.

Skamarock, W. C., and Coauthors, 2008: A description of the Advanced Research WRF version 3. NCAR Tech. Note NCAR/TN-475+STR, 113 pp., https://doi.org/10.5065/D68S4MVH.

Sobash, R. A., and D. J. Stensrud, 2013: The impact of covariance localization for radar data on EnKF analyses of a developing MCS: Observing system simulation experiments. *Mon. Wea. Rev.*, **141**, 3691–3709, https://doi.org/10.1175/MWR-D-12-00203.1.

Steiner, M., 2019: Urban air mobility: Opportunities for the weather community. *Bull. Amer. Meteor. Soc.*, **100**, 2131–2133, https://doi.org/10.1175/BAMS-D-19-0148.1.

Sun, Q., T. Vihma, M. O. Jonassen, and Z. Zhang, 2020: Impact of assimilation of radiosonde and UAV observations from the Southern Ocean in the polar WRF model. *Adv. Atmos. Sci.*, **37**, 441–454, https://doi.org/10.1007/s00376-020-9213-8.

Tesfuhuney, W., S. Walker, L. van Rensburg, and C. Everson, 2013: Water vapor, temperature and wind profiles within maize canopy under in-field rainwater harvesting with wide and narrow runoff strips. *Atmosphere*, **4**, 428–444, https://doi.org/10.3390/atmos4040428.

Torn, R. D., and G. J. Hakim, 2008: Performance characteristics of a pseudo-operational ensemble Kalman filter. *Mon. Wea. Rev.*, **136**, 3947–3963, https://doi.org/10.1175/2008MWR2443.1.

Vömel, H., and Coauthors, 2018: NCAR/EOL Community workshop on unmanned aircraft systems for atmospheric research. NCAR Earth Observing Laboratory Tech. Rep., 83 pp, https://doi.org/10.5065/D6X9292S..

Waugh, S., 2020a: National Severe Storms Laboratory mobile soundings during lapse-rate. Zenodo, accessed 5 August 2020, https://doi.org/10.5281/zenodo.3720342.

——, 2020b: National Severe Storms Laboratory mobile soundings during LAPSE-RATE (CLAMPS trailer). Zenodo, accessed 5 August 2020, https://doi.org/10.5281/zenodo.3720444.

Whiteman, C. D., 2000: *Mountain Meteorology: Fundamentals and Applications*. Oxford University Press, 376 pp.

Wilczak, J., and Coauthors, 2015: The Wind Forecast Improvement Project (WFIP): A publiic-private partnership addressing wind energy forecast needs. *Bull. Amer. Meteor. Soc.*, **96**, 1699–1718, https://doi.org/10.1175/BAMS-D-14-00107.1.

Wong, M., G. Romine, and C. Snyder, 2020: Model improvement via systematic investigation of physics tendencies. *Mon. Wea. Rev.*, **148**, 671–688, https://doi.org/10.1175/MWR-D-19-0255.1.